UNIVERSIDADE FEDERAL FLUMINENSE

LUCAS PRATA FERREIRA

AN IMAGE-BASED NUMERICAL HOMOGENIZATION STRATEGY FOR CHARACTERIZATION OF VISCOELASTIC HETEROGENEOUS MATERIALS

NITERÓI

2022

LUCAS PRATA FERREIRA

AN IMAGE-BASED NUMERICAL HOMOGENIZATION STRATEGY FOR CHARACTERIZATION OF VISCOELASTIC HETEROGENEOUS MATERIALS

Dissertation presented to the Graduate Program in Computing of the Universidade Federal Fluminense as partial requirement for obtaining the Degree of Master in Computing. Area of concentration: Computer Science.

Advisor:
DR. ANDRÉ MAUÉS BRABO PEREIRA

Co-advisor:
DR. RICARDO LEIDERMAN

NITERÓI

2022

Ficha catalográfica automática - SDC/BEE
Gerada com informações fornecidas pelo autor

F383a Ferreira, Lucas Prata
An Image-based Numerical Homogenization Strategy fo Characterization of Viscoelastic Heterogeneous Materials / Lucas Prata Ferreira ; André Maués Brabo Pereira, orientador ; Ricardo Leiderman, coorientador. Niterói, 2022.
79 f. : il.

Dissertação (mestrado)-Universidade Federal Fluminense, Niterói, 2022.

DOI: http://dx.doi.org/10.22409/PGC.2022.m.15046579774

1. Viscoelasticidade. 2. Modelagem computacional. 3. Produção intelectual. I. Pereira, André Maués Brabo, orientador. II. Leiderman, Ricardo, coorientador. III. Universidade Federal Fluminense. Instituto de Computação. IV. Título.

CDD -

Bibliotecário responsável: Debora do Nascimento - CRB7/6368

LUCAS PRATA FERREIRA

AN IMAGE-BASED NUMERICAL HOMOGENIZATION STRATEGY FOR CHARACTERIZATION OF VISCOELASTIC HETEROGENEOUS MATERIALS

Dissertation presented to the Graduate Program in Computing of the Universidade Federal Fluminense as partial requirement for obtaining the Degree of Master in Computing. Area of concentration: Computer Science.

Approved in July of 2022.

EXAMINATION BOARD

Andre Maues Brabo Pereira
Andre Maues Brabo Pereira (Jul 29, 2022 12:42 ADT)

Prof. Dr. André Maués Brabo Pereira - Advisor, UFF

Ricardo L
Ricardo Leiderman (Jul 29, 2022 13:52 ADT)

Prof. Dr. Ricardo Leiderman - Co-advisor, UFF

Prof. Dr. Daniel Cardoso Moraes de Oliveira, UFF

Francisco Thiago Sacramento Aragão
Francisco Thiago Sacramento Aragão (Jul 29, 2022 15:03 ADT)

Prof. Dr. Francisco Thiago Sacramento Aragão, UFRJ

Prof. Dr. Daniel Alves Castello, UFRJ

Niterói

2022

Resumo

Uma abordagem simples e direta é apresentada para caracterizar materiais heterogêneos viscoelásticos diretamente no domínio do tempo. Os módulos de relaxação homogeneizados são encontrados em instantes discretos aplicando um campo de deformação constante a um elemento de volume representativo do material heterogêneo. As curvas-mestras de relaxação são então ajustadas via um problema de otimização usando o modelo de Maxwell generalizado representado pela série de Prony. O esquema usa uma imagem digital de uma amostra, onde cada voxel corresponde a um elemento na formulação de elementos finitos, o que reduz dramaticamente a exaustiva tarefa de discretização do domínio, e ao mesmo tempo, utiliza as cores dos voxels como identificadores dos materiais. Condições de contorno periódicas são aplicadas para modelar um meio infinitamente periódico. Uma estratégia sem montagem de matrizes é empregada para resolver os sistemas de equações com um método iterativo. A quantidade de memória necessária para resolver o problema usando o esquema proposto é drasticamente menor do que o necessário com um solver direto, possibilitando a solução de problemas grandes com centenas de milhões de graus de liberdade usando computadores pessoais ordinários. Exemplos em 2-D e 3-D são analisados para verificar a efetividade do esquema, assim como para validar a formulação e a implementação. Foram caracterizadas três misturas de concreto asfáltico a partir de imagens de micro CT por raios-X para demonstrar a aplicabilidade real do esquema. Os resultados capturaram bem a natureza anisotrópica dos modelos, bem como a variação esperada no comportamento de relaxação, dadas as diferentes razões entre constituintes elásticos e viscoelásticos.

Keywords: viscoelasticidade, homogeneização, domínio do tempo, análise baseada em imagens, homogeneizaçao numérica, método dos elementos finitos

Abstract

A simple and straightforward image-based approach is introduced to characterize viscoelastic heterogeneous materials directly in the time domain. The homogenized relaxation moduli are found at discrete instants by applying a constant strain field to a representative volume element of the heterogeneous material. The relaxation master curves are then adjusted via an optimization problem using the generalized Maxwell model represented by the Prony series. The scheme uses a digital sample image in which each voxel corresponds to a finite element in the finite element formulation, dramatically reducing the time-consuming task of meshing the domain, while also using the voxel colors as material identifiers. Periodic boundary conditions are applied to model an infinitely periodic medium, and an assembly-free strategy to solve the systems of equations on-the-fly using an iterative method is employed to avoid storing the whole stiffness matrix. The amount of memory necessary to solve the problem using the scheme proposed here is drastically smaller than the needed with a direct solver, enabling the solution of large problems with hundreds of millions of degrees of freedom using ordinary personal computers. 2-D and 3-D examples are analyzed to verify the scheme's effectiveness and validate the formulation as well as the implementation. X-ray micro-CT images from three mixtures of asphaltic concrete were characterized to demonstrate the real applicability of the proposition. The results captured well the anisotropic nature of the models and the expected variation in the relaxation behavior given different ratios of elastic to viscoelastic constituents was observed as well.

Keywords: viscoelasticity, homogenization, time domain, image-based analysis, numerical homogenization, finite element method

List of Figures

List of Tables

Contents

1 Introduction

1.1 Contextualization

Composites are heterogeneous materials that are commonly used in a wide range of applications, such as space structures, sports equipment and medical tools. The growing number of composite types and their applications is due to the fact that in many cases they present mechanical characteristics their constituents can't offer individually. Besides, a great range of composites is partially made out of otherwise waste materials (e.g. recycled rubber in some mixtures of asphaltic concrete), what helps mitigate the environmental impact caused by the industry in general.

To attain the best possible characteristics out of a manufactured composite, the volume ratio between different constituents, as well as their geometrical arrangement and distribution must be carefully determined. A large part of the composites used nowadays are apparently homogeneous to the human eye, but are highly heterogeneous at lengths ranging from very little to imperceptible to human sight. These two different scales of measurement will be henceforth called macroscale and microscale, and are defined relatively to one another, not in absolute measures. In that sense, the property desired from a composite must be determined taking in account the heterogeneities, in whatever absolute scale they are. These types of analysis are said multiscale problems, because they perceive the connection between different scales. Multiscale models of manufactured composites must, then, be capable of containing as much information as possible from the microscale, so the maximum number of variables are under control of the designer of the then-to-be homogenized composite material. Conceptually, the microscale is defined as a scale in which a field ϕ described in the domain Ω varies greatly and abruptly. The macroscale, on the other hand, has the same field varying smoothly. That is, in the macroscale, the absolute size of the heterogeneities is much smaller than the characteristic wave length of the excitation that generates ϕ.

For the characterization of a structural material, the most important property that

must always be determined is its stiffness, which may vary depending on the circumstances. Many manufactured composites are considered viscoelastic because they present a time-dependent response to loading due to the viscoelastic nature of one or more of their constituents. On account of the long-term effects of creep and relaxation in the homogenized stiffness, proper characterization is vital in developing materials that must be operational for a long period.

1.2 Motivations

The physical tests that characterize viscoelastic materials generally involve the application of dynamic loads with different frequencies and at different temperatures. The material response is measured, the parameters that describe the mechanical properties are calculated and, if necessary, analytically converted to a convenient domain. Nevertheless, most of the advancements on approaching viscoelastic characterization of heterogeneous media are not only executed on the Laplace-Carson domain, which is numerically expensive, as discussed in Chapter 3, but are also highly inefficient in terms of managing computational resources. An attractive alternative to the problem is performing the characterization directly on the time domain. In addition, the need for detail of the microstructural modeling requires strategies to make feasible the solution of such huge problems.

Despite precision in manufacturing, industrial composites are never completely regular and are highly heterogeneous on the microscale, making it virtually impossible to find analytical solutions for homogenization problems taking into account the actual geometry. In this scenario, the microstructural arrangement is of major importance in performing an accurate characterization. Imaging is a convenient strategy to acquire these arrangement architectures, and it can be executed with various techniques. When associated with numerical methods, the images can serve as a great tool to properly describe composite media.

In the light of the above, an optimum way to numerically characterize viscoelastic composites is using images to create a digital model, and performing the homogenization procedures needed directly in the time domain. This window of opportunity for development is explored in this work.

1.3 Literature review

The first efforts in developing a procedure for homogenizing viscoelastic properties took advantage of the correspondence principle between linear elastic and viscoelastic behavior, as in [13] and [5]. In this procedure, the effective relaxation and creep viscoelastic functions are translated to the Laplace-Carson (LC) space as linear elastic moduli. The homogenization can then be performed analytically and the results are transformed back to the time domain. Many homogenization methods based on the correspondence principle have been used to characterize viscoelastic materials, such as the self-consistent [14] and Mori-Tanaka [25] models, making them the most common approaches to solve the problem. In addition, for simple periodic microstructures, analytical solutions can be found using the concept of Representative Volume Element with Periodic Boundary Conditions (PBC), as done in [20], [4], and [33]. However, real composite materials usually present an intricate microstructural geometry, making the analytical solutions inapplicable. Although the transformation from the time domain to the LC domain is straightforward, the inverse transform is in general performed numerically. This inverse transform is costly and comes at the price of accuracy and stability, as it is ill-conditioned [38]. Moreover, the whole response and loading history is necessary to perform the analyses. In this sense, the homogenization directly in the time domain is preferable, as the viscoelastic models are explicitly described in it.

There have been some recent advances in the field of viscoelastic homogenization in time domain. To overcome the need for storing the whole response and loading history, internal variable approaches were developed, such as the one employed by Coulibaly and Sabar [7]. In their approach, all the memory effects at a future instant t_{n+1} are provided by known incremental variables at a current instant t_n, which are then updated. Despite the great simplification when compared to LC schemes, the internal variable approach still needs to store data from the previous time step to calculate the following. This is not necessary for the scheme proposed in this work, because while the calculations are also performed in discrete instants, they are completely independent of each other. With a variational formulation, Tang et al. [42] propose a method for finding the effective relaxation modulus directly in the time domain by specifying boundary conditions in a representative volume element of polymer composites. Although the model proposed in [42] can be applied to polymer composites having any shape of reinforcements, they could only solve a simple fiber-reinforced composite. The proposed scheme here not only is capable of handling any sort of heterogeneity captured by the images, but also is

efficient in terms of memory consumption, making possible the analysis of large models in otherwise incapable machines. For further insight on homogenization procedures, an extensive literature review on the subject is presented in [31].

Images are a great mean for representing material microstructure, and many imaging techniques are already applied to support the numerical determination of physical properties, e.g. X-ray micro-CT scans are used by NASA in the PuMA software [9] to determine various properties. This imaging technique is highly adopted by the community, especially when analyzing materials with complex geometry due to its capability of achieving high resolutions. Indeed, micro-CT scans have already been applied to viscoelastic material characterization. In [47], the images are used to create 2D and 3D models for determining the homogenized dynamic modulus of asphalt concrete using the Discrete Element Method (DEM). In [8], the same procedures is performed, but using the Finite Element Method (FEM). Ying [45] also does a dynamic modulus homogenization, and demonstrates that the models based on micro-CT scans perform well also when executing analyses at a wide range of temperatures and frequencies.

What most of the works on the field have in common is the fact that they generally use a commercial platform to solve the problem, the most popular one being Abaqus [42, 37, 16, 46, 8, 45]. Even though the utilized subroutines are user-defined, the software's solver is a black box that blinds the user from how the calculations are executed. This inhibits proper memory control and may induce greater computation time than needed.

1.4 Main contribution

The aim of this work is to introduce a scheme in which the homogenized property is the effective constitutive relaxation matrix. The homogenization procedure is performed directly in the time domain, at discrete instants, turning the transient viscoelastic problem into a series of elastostatic ones. This strategy avoids the need of storing all the viscoelastic memory effects. The FE problem is discretized in a voxel-based manner, and is solved using the assembly-free element-by-element procedure, which opens doors to massively parallelizable implementations and the possibility of running large models. After the homogenization, a least squares curve adjustment method is used to determine the Prony series parameters describing a generalized Maxwell viscoelastic model. The image-based scheme proposed here is a technological novelty in the sense that it bridges the well-established elastostatic homogenization procedure to the determination of

viscoelastic properties without the use of numerical transformations between domains. The voxel-based meshing, besides entailing a great economy in computational effort, also makes possible the best geometric description possible of the model. Most of the previous attempts to the viscoelastic homogenization directly in the time domain, because of the commercial platforms used, can only handle simple geometries that don't properly represent real materials.

1.5 Structure of the work

The rest of the work is organized as follows. Chapter 2 showcases all the theoretical fundamentals needed for the development of this work. Basic notions of the FEM, the theory of viscoelasticity, and homogenization concepts are presented. Chapter 3 elucidates how the FE algorithm for proposed scheme was developed, its characteristics, and computational aspects of the implementation. In Chapter 4, two numerical problems with synthetic models are unraveled to verify and exemplify the algorithm's solutions. Chapter 5 demonstrates the application of the scheme to real materials, and validates the results by comparing the numerical solutions to experimental data for an example with asphaltic concrete. Finally, Chapter 6 draws the conclusions on the work contents.

2 Theoretical foundations

This chapter presents the theoretical background necessary for the development of the work. All the mathematical fundamentals are described and elucidated here. The chapter is divided in three sections, those being: 2.1) Viscoelasticity, 2.2) The Finite Element Method, and 2.3) Homogenization Theory.

2.1 Viscoelasticity

The most common approach to structural analysis consider the employed materials as always within the linear elastic regime, in which the internal energy is not dissipated and deformations are completely recoverable. However, some materials show different mechanical behaviors when loaded for a long period of time. The time dependency in the response of these materials is due to their viscoelastic nature.

In elastic solids the stress state within a body at an instant $t_0 > 0$ is a simple function of the strain state at that instant t_0. On the other hand, in viscoelastic solids the stress state at the same instant $t_0 > 0$ is a function of the strain state and strain rate at instant t_0, as well as of the history of strains, that is, the past strain states and strain rates when $t < t_0$. The viscoelastic behavior is a combination of elastic bearing, that permits recoverable deformations, and viscous flow, that allows only for unrecoverable deformations. However, the response is not as simple as the sum of the elastic strain to the viscous strain [2]. To represent the complex response, many different viscelastic models have been created over the years. In this work, only linear viscoelastic models will be presented.

Schapery [35] presents a concise explanation of the linearity concept in viscoelasticity. Let

$$R = \{I\} \quad , \tag{2.1}$$

where R is the response of a material subject to an input load I, such that the curly

brackets { } imply that the current value of R is not a simple function of I, but a function of the history of I. R is called a functional of I, and is linear if, and only if, the following two conditions are satisfied:

$$\begin{aligned} &(i) \quad \text{proportionality} && R\{cI\} = cR\{I\} \quad , \\ &(ii) \quad \text{superposition} && R\{I_a + I_b\} = R\{I_a\} + R\{I_b\} \quad , \end{aligned} \tag{2.2}$$

where c is a constant and I_a and I_b can be either the same or different input loads. All materials that satisfy (i) and (ii) are considered linearly viscoelastic. It is also stated in [35] that if the condition (ii) is satisfied, so is condition (i), but the reciprocal is not true.

2.1.1 Constitutive relations of linear viscoelasticity

The deduction of the viscoelastic constitutive relations presented in this subsection are done for the one-dimensional case, but extension to higher dimensions can be done intuitively.

The two most common approaches to viscoelastic characterization of materials are the physical tests that measure the phenomena of creep and relaxation. In the creep, a constant stress load σ_0 is applied to a sample for a certain amount of time, and the strain response $\varepsilon(t)$ is measured to find the creep compliance $D(t)$ of the material with the relation:

$$D(t) = \frac{\varepsilon(t)}{\sigma_0} \quad . \tag{2.3}$$

The relaxation test, on the other hand, is executed by applying a constant strain ε_0 to a sample for a certain period and measuring the stress relaxation $\sigma(t)$ over time, thus arriving to the relaxation modulus $E(t)$ with the relation:

$$E(t) = \frac{\sigma(t)}{\varepsilon_0} \quad . \tag{2.4}$$

In elastic solids these two quantities are the inverse of one another, but when they change in time, as in viscoelasticity, their connection is more complex.

For simplification purposes, this work will only handle non-ageing viscoelastic behavior, which means that the mechanical response of the material is a function of only the duration of the load. In other words, considering that the load begins being applied at instant $\tau \geq 0$, the stress state at instant $t > \tau$ denoted by $\sigma(t)$ is a function of only $t - \tau$, hence:

$$\sigma(t) = E(t - \tau)\varepsilon_0 \quad , \tag{2.5}$$

with $E(t<0)=0$.

Being $\varepsilon(t)$ an arbitrary strain load, it can be decomposed as a sum of unitary strain loads in the form of a Heaviside function applied at different instants τ_i, as illustrated in Figure 2.1.

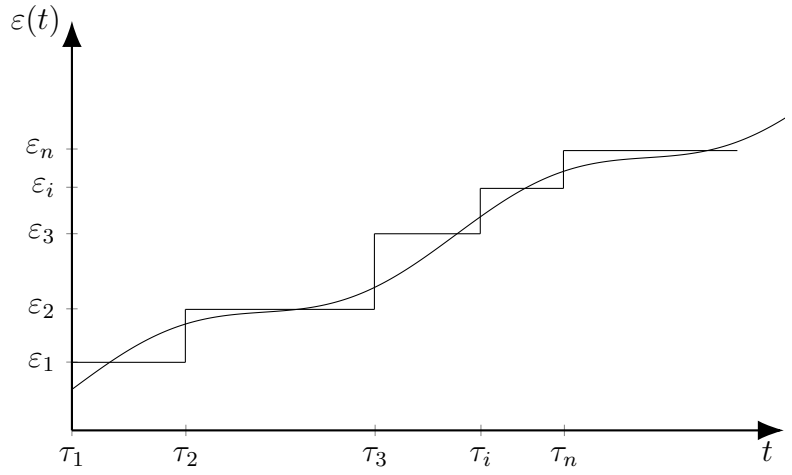

Figure 2.1: Decomposition of an arbitrary $\varepsilon(t)$ load into various loads in the form of a sum of Heaviside functions.

With this decomposition, the superposition principle can be applied to find the response:

$$\sigma(t) = E(t-\tau_1)\varepsilon_1 + E(t-\tau_2)(\varepsilon_2-\varepsilon_1) + \cdots + E(t-\tau_n)(\varepsilon_n-\varepsilon_{n-1}) = \sum_{i=1}^{n} E(t-\tau_i)(\varepsilon_i-\varepsilon_{i-1}) \quad . \tag{2.6}$$

Limiting ε_i to be infinitesimally small, considering the first load increment at $\tau = 0$, and dividing and multiplying the right-hand side of Equation 2.6 by $d\tau_i$ gives:

$$\begin{gathered} \sigma(t) = \lim_{\varepsilon_i \to 0} \sum_{i=1}^{n} E(t-\tau_i) \frac{\varepsilon_i}{d\tau_i} \; d\tau_i \\ \therefore \; \sigma(t) = \int_0^t E(t-\tau) \frac{\partial \varepsilon}{\partial \tau} \; d\tau \quad . \end{gathered} \tag{2.7}$$

In an analogous way, the creep compliance can be deducted to find:

$$\varepsilon(t) = \int_0^t D(t-\tau) \frac{\partial \sigma}{\partial \tau} \; d\tau \quad . \tag{2.8}$$

Consider now a simple algebraic manipulation of Equation 2.4 in the case of a rela-

xation test, with reference to the initial instant of the test:

$$\sigma(\tau) = \varepsilon_0 E(\tau) \quad . \tag{2.9}$$

Differentiating Equation 2.9 with respect to τ gives:

$$\frac{d\sigma(\tau)}{d\tau} = \varepsilon_0 \frac{dE(\tau)}{d\tau} \quad . \tag{2.10}$$

Now, substituting Equation 2.10 in Equation 2.8:

$$\begin{aligned} \varepsilon(t) &= \int_0^t D(t-\tau)\varepsilon_0 \frac{dE(\tau)}{d\tau} \ d\tau \\ \therefore \int_0^t D(t-\tau)\frac{dE(\tau)}{d\tau} \ d\tau &= 1 \qquad \text{for } t > 0 \quad , \end{aligned} \tag{2.11}$$

which can be rewritten [10] as

$$\int_0^t D(t-\tau) dE(\tau) \ d\tau = t \qquad \text{for } t > 0 \quad . \tag{2.12}$$

With a similar deduction, one can arrive to:

$$\int_0^t E(t-\tau) dD(\tau) \ d\tau = t \qquad \text{for } t > 0 \quad . \tag{2.13}$$

From Equations 2.12 and 2.13, in accord with the superposition principle [10], it follows:

$$E(t)D(t) \leq 1 \quad . \tag{2.14}$$

Equation 2.14 demonstrates that, even though the relaxation modulus and the creep compliance are directly related, they are not reciprocal as in the linear elastic regime. Equations 2.12 and 2.13 show that these two quantities that represent the constitutive viscelastic properties are related through a convolution integral.

As problems with viscoelastic materials involve solving integrals and differential equations, their exact solutions are troublesome and at times impossible. To contour this, both numerical and analytical mathematical strategies have been developed. The most common ones are the Laplace-Carson (LC) Transform and the Fast Fourier Transformation (FFT), being the second generally applied to problems with harmonic loading cases [41].

The elastic-viscoelastic correspondence principle states that viscoelastic problems can

be much more easily solved if taken to another mathematical domain. A viscoelastic problem in the time domain becomes a correspondent similar elastic problem once transformed to the LC domain, for instance. The viscoelastic functions must be transformed to the LC domain, making the constitutive equation of the material linear, as in elastic cases. Mathematically, this means that the Equation 2.14 becomes, in the LC domain, an equity:

$$\tilde{E}\tilde{D} = 1 \quad , \tag{2.15}$$

where $\tilde{E}$ is the LC transform of the relaxation modulus, and $\tilde{D}$ is the LC transform of the creep compliance, which are equal to the relaxation modulus and creep compliance in the Laplace domain multiplied by the complex variable s, respectively. The viscoelastic solution is then found with the inverse LC transformation of the elastic solution [6].

The LC transform of Equation 2.7 is:

$$\overline{\sigma} = \tilde{E}\,\overline{\varepsilon} \quad , \tag{2.16}$$

where $\overline{\sigma}$ is the stress state in the Laplace domain, and $\overline{\varepsilon}$ is the strain state in the Laplace domain. Equation 2.16 illustrates clearly how viscoelastic problems are correspondent to elastic problems in changed domains.

2.1.2 Viscoelastic models

The viscoelastic models were developed to explain mathematically experimental data obtained from tests with viscoelastic materials. Evidently, some of the models are better fits to certain materials and conditions than others. Most of the models are expressed mathematically in a way that can be explained with mechanical analogues. Specifically, different associations between springs and dashpots. This sort of representation has two main advantages: it gives physical meaning to the parameters as spring stiffnesses or dashpot viscosities, and it mostly involves exponential functions that can be easily integrated [41]. The models presented in this subsection are also for one-dimensional problems, but the expansion to higher dimensions is easily done intuitively.

The most simple models are the Maxwell and Voigt models, illustrated in Figure 2.2 a and b, respectively. These simple arrangements of a single spring connected to a single dashpot, in series in the Maxwell model, and in parallel in the Voigt model, are already capable of capturing the time-dependent behavior of the materials, but during a brief period of time. To better represent materials that change response over a long period,

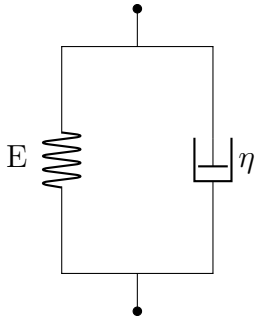

(a) The Maxwell model.

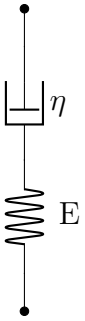

(b) The Voigt model.

Figure 2.2: The most simple linear viscoelastic models.

more complex models are necessary. The models generally adopted to describe viscoelastic solids are the generalized Maxwell model and the generalized Voigt model, illustrated in Figure 2.3 a and b, respectively. They are commonly called standard solid models.

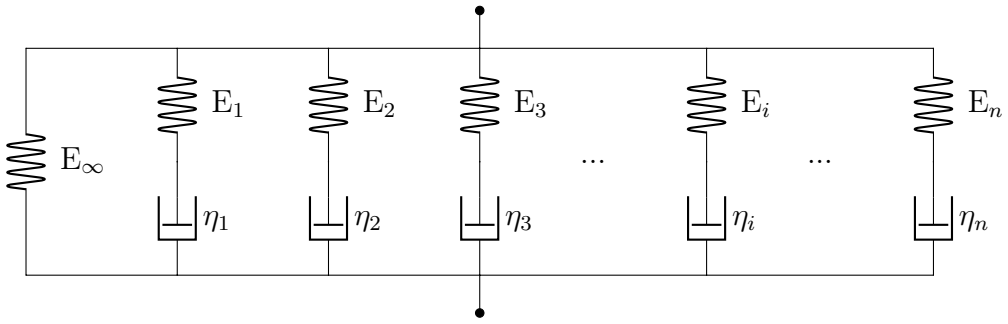

(a) The generalized Maxwell model.

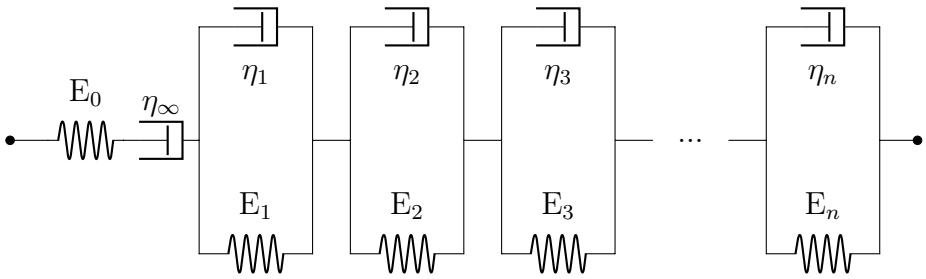

(b) The generalized Voigt model.

Figure 2.3: Standard solid models.

The two generalized models are equivalent [39], but the mathematical representation of the relaxation phenomenon is better expressed by the generalized Maxwell model, while creep is better described by the generalized Voigt model. Both models are associations of simple Maxwell and Voigt elements in parallel or in series, with each element addition to the chain differing only in the physical properties of the spring and dashpot, in order to cover with more detail the period of time analyzed.

Both generalized models can be expressed mathematically using a Prony series. The formulation of the relaxation modulus $E(t)$ with the generalized Maxwell model is:

$$E(t) = E^{\infty} + \sum_{i=1}^{n} E^i \, e^{-\frac{t}{\tau^i}} \quad , \tag{2.17}$$

where E^{∞} is the elastic constant of the sole spring in parallel to the other Maxwell elements, called the long-term modulus, n is the total number of Maxwell elements in the model analyzed, E^i is the stiffness of the spring in the i-th element, and τ^i is called the relaxation time of the i-th element, which is found with the relation below:

$$\tau_i = \frac{\eta^i}{E^i} \quad , \tag{2.18}$$

where η^i is the dashpot viscosity of the i-th element.

Equation 2.17 can be rewritten in terms of an instantaneous modulus E^0 as:

$$E(t) = E^0 + \sum_{i=1}^{n} E^i \, (1 - e^{-\frac{t}{\tau^i}}) \quad , \tag{2.19}$$

with $E^0 = E^{\infty} + \sum_{i=1}^{n} E^i$.

The creep compliance $D(t)$, when adopting the generalized Voigt model, is described similarly:

$$D(t) = D^0 + \frac{t}{\eta^{\infty}} + \sum_{j=1}^{n} D^j \, (1 - e^{-\frac{t}{\rho^j}}) \quad , \tag{2.20}$$

such that:

$$\begin{aligned} D^0 &= \frac{1}{E^{\infty}} \quad , \\ D^j &= \frac{1}{E^j} \quad , \\ \rho^j &= \eta^j D^j \quad . \end{aligned} \tag{2.21}$$

It is important to note that, according to Park and Schapery [28], for any viscoelastic solid, $E_{\infty} > 0$ and $\eta_{\infty} \to \infty$.

An advantage of the Prony series representation of viscoelastic materials is that once all the parameters of Equations 2.17 and 2.20 are determined, the properties can be directly converted to both the frequency domain (ω) and the Laplace space (s). In the equations below, presented by Park and Schapery [28], the single apostrophe ($'$) and double apostrophe ($''$) signs designate, respectively, the real and the imaginary parts of

their respective complex functions.

$$E'(\omega) = E^{\infty} + \sum_{i=1}^{n} \frac{\omega^2 \tau^{i2} E^i}{\omega^2 \tau^{i2} + 1} \quad , \tag{2.22}$$

$$E''(\omega) = \sum_{i=1}^{n} \frac{\omega \tau^i E^i}{\omega^2 \tau^{i2} + 1} \quad , \tag{2.23}$$

$$D'(\omega) = D^0 + \sum_{j=1}^{n} \frac{D^j}{\omega^2 \rho^{j2} + 1} \quad , \tag{2.24}$$

$$D''(\omega) = \frac{1}{\eta^{\infty} \omega} + \sum_{j=1}^{n} \frac{\omega \rho^j D^j}{\omega^2 \rho^{j2} + 1} \quad , \tag{2.25}$$

$$\tilde{E}(s) = E^{\infty} + \sum_{i=1}^{n} \frac{s \tau^i E^i}{s \tau^i + 1} \quad , \tag{2.26}$$

$$\tilde{D}(s) = D^0 + \frac{1}{\eta^{\infty} s} + \sum_{j=1}^{n} \frac{D^j}{s \rho^j + 1} \quad . \tag{2.27}$$

To adjust experimental data to the mathematical description of the chosen viscoelastic model, the best set of parameters that satisfy Equations 2.17 and 2.20 must be determined. For that matter, one must analyze the nature of the mathematical representation that will adjust the data. The Prony series is a sum of simple exponential functions, implying that it behaves qualitatively as an exponential function, but with a larger domain of variation.

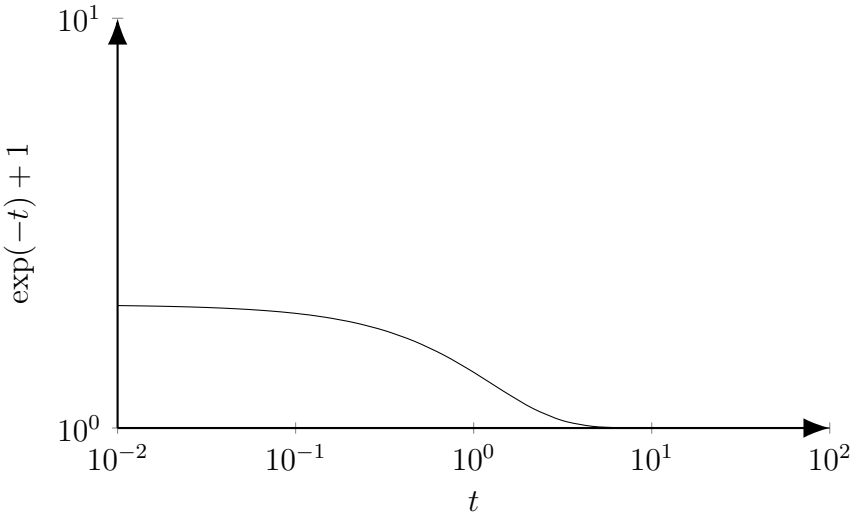

Figure 2.4: Behavior of a simple exponential function in the log-log scale.

Figure 2.4 illustrates the behavior of a simple exponential function in the form $f(t) =$

$e^{-\frac{t}{a}} + b$. The value of 10 was adopted to a and 1 to b in order to better showcase the shape of the curve in the log-log scale. It is clear that the variation of f is not only centered in a, but it is much more pronounced within two decades than in the rest of the curve. That is, roughly, f varies solely between the decade immediately before the order of magnitude of a, and the decade after the order of magnitude of a. In that sense, to generate, from a sum of simple exponential functions, a smooth exponential function with a larger domain of variation than a simple one, the a parameter in these summed functions must differ in no more than one decade from each other.

2.2 The Finite Element Method

The Finite Element Method (FEM) is, conceptually, "a general discretization procedure of continuum problems posed by mathematically defined statements"[48]. That is, in other words, a mathematical procedure to approximate the solution of a continuous domain problem with infinite unknown variables by solving an analogue problem consisting of a finite set of subdomains, the finite elements, with a finite number of unknown variables (degrees of freedom). Each element is analyzed on its own and the whole problem is solved, in structural analysis problems, by imposing compatibility of displacements and equilibrium at the boundary between elements.

The elements are solved individually by the adoption of shape functions that approximate the solution within them, using the values at their boundaries. The higher the degree of the shape functions adopted, the more refined the domain discretization must be, as the interpolation is done between certain points of the element boundaries, the nodes. The most simple shape function, a linear function, requires at least two nodes, quadratic functions require three, cubic functions need four, and so on. The values at the nodes are calculated by solving a system of equations in which they are the unknowns. In essence, the method transforms the solution of a problem that would originally involve differential equations into a system of algebraic equations.

In static analysis, for each element e, the equilibrium equation is valid:

$$\mathbf{k}_e \mathbf{d}_e = \mathbf{f}_e \quad , \tag{2.28}$$

where $\mathbf{d}_e$ is the vector of nodal displacements, $\mathbf{f}_e$ is the vector of nodal loads, and $\mathbf{k}_e$ is the element's stiffness matrix, obtained in the global reference system of coordinates by

solving the following integral over the element's volume:

$$\mathbf{k}_e = \int_{V_e} \mathbf{B}_e^T \mathbf{C}_e \mathbf{B}_e \ dV_e \quad , \tag{2.29}$$

where V_e is the volume of the element, $\mathbf{C}_e$ is the material's constitutive matrix, and $\mathbf{B}_e$ is the matrix that relates strain to nodal displacements, henceforth called $\mathbf{B}$ matrix. The constitutive matrix carries the physical properties of the material, and is determined in accord with the type of problem analyzed (plane strain, plane stress, axisymmetric, etc.). The $\mathbf{B}$ matrix, on the other hand, is based on the shape functions, thus being directly dependent on the type of the element. The approach presented in this work uses only the isoparametric formulations of the bilinear square element and trilinear hexahedral element for 2-D and 3-D cases, respectively. A brief explanation on the bilinear square element is presented next, and the extension to the trilinear hexahedral element is intuitive and straightforward.

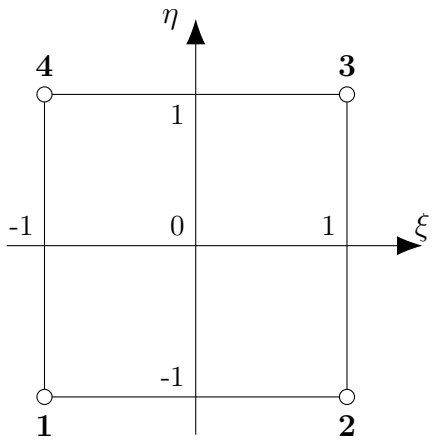

Figure 2.5: A regular Quad4 element.

Figure 2.5 illustrates a regular bilinear square element with the indication of the normalized local coordinate system (ξ, η). The problem to be solved is two dimensional, so each node has two degrees of freedom (DOF), horizontal and vertical displacements, being eight in total for the element. The displacements within the element are approximated using bilinear shape functions that guarantee continuity within the element and linearity of the interpolation along the edges [11]. Each node has one shape function related to it, and the interpolation of the displacement at a certain point is equal to the sum of the shape functions evaluated at that point multiplied by the associated node displacement.

The shape functions N for each node are:

$$\begin{aligned} N_1(\xi,\eta) &= \frac{1}{4}(\xi-1)(\eta-1) \quad , \\ N_2(\xi,\eta) &= -\frac{1}{4}(\xi+1)(\eta-1) \quad , \\ N_3(\xi,\eta) &= \frac{1}{4}(\xi+1)(\eta+1) \quad , \\ N_4(\xi,\eta) &= -\frac{1}{4}(\xi-1)(\eta+1) \quad , \end{aligned} \tag{2.30}$$

such that at any point within the element, the horizontal and vertical displacements $u(\xi,\eta)$ and $v(\xi,\eta)$, respectively, are interpolated from the nodal displacements u_i and v_i contained in $\mathbf{d}_e$ as:

$$\begin{aligned} u(\xi,\eta) &= u_1N_1(\xi,\eta) + u_2N_2(\xi,\eta) + u_3N_3(\xi,\eta) + u_4N_4(\xi,\eta) \quad , \\ v(\xi,\eta) &= v_1N_1(\xi,\eta) + v_2N_2(\xi,\eta) + v_3N_3(\xi,\eta) + v_4N_4(\xi,\eta) \quad . \end{aligned} \tag{2.31}$$

In matricial form, Equation 2.31 reads:

$$\begin{bmatrix} u \\ v \end{bmatrix} = \begin{bmatrix} N_1 & 0 & N_2 & 0 & N_3 & 0 & N_4 & 0 \\ 0 & N_1 & 0 & N_2 & 0 & N_3 & 0 & N_4 \end{bmatrix} \begin{bmatrix} u_1 \\ v_1 \\ u_2 \\ v_2 \\ u_3 \\ v_3 \\ u_4 \\ v_4 \end{bmatrix} \quad . \tag{2.32}$$

The $\mathbf{B}$ matrix is defined with respect to the global coordinate system (x, y):

$$\mathbf{B} = \begin{bmatrix} \frac{\partial N_1}{\partial x} & 0 & \frac{\partial N_2}{\partial x} & 0 & \frac{\partial N_3}{\partial x} & 0 & \frac{\partial N_4}{\partial x} & 0 \\ 0 & \frac{\partial N_1}{\partial y} & 0 & \frac{\partial N_2}{\partial y} & 0 & \frac{\partial N_3}{\partial y} & 0 & \frac{\partial N_4}{\partial y} \\ \frac{\partial N_1}{\partial y} & \frac{\partial N_1}{\partial x} & \frac{\partial N_2}{\partial y} & \frac{\partial N_2}{\partial x} & \frac{\partial N_3}{\partial y} & \frac{\partial N_3}{\partial x} & \frac{\partial N_4}{\partial y} & \frac{\partial N_4}{\partial x} \end{bmatrix} . \tag{2.33}$$

such that the strain vector $\boldsymbol{\varepsilon}$ is calculated as:

$$\boldsymbol{\varepsilon} = \begin{bmatrix} \varepsilon_{xx} \\ \varepsilon_{yy} \\ \gamma_{xy} \end{bmatrix} = \mathbf{B}\mathbf{d}_e \quad , \tag{2.34}$$

and the vector of stresses $\boldsymbol{\sigma}$ is expressed as:

$$\boldsymbol{\sigma} = \begin{bmatrix} \sigma_{xx} \\ \sigma_{yy} \\ \tau_{xy} \end{bmatrix} = \mathbf{C}_e\boldsymbol{\varepsilon} = \mathbf{C}_e\mathbf{B}\mathbf{d}_e \quad . \tag{2.35}$$

However, the shape functions are defined at the local coordinate system. So, in order to find their derivatives in relation to the global coordinate system to build $\mathbf{B}$, the chain rule must be applied:

$$\begin{aligned} \frac{\partial N_i}{\partial \xi} &= \frac{\partial N_i}{\partial x}\frac{\partial x}{\partial \xi} + \frac{\partial N_i}{\partial y}\frac{\partial y}{\partial \xi} \quad , \\ \frac{\partial N_i}{\partial \eta} &= \frac{\partial N_i}{\partial x}\frac{\partial x}{\partial \eta} + \frac{\partial N_i}{\partial y}\frac{\partial y}{\partial \eta} \quad , \end{aligned} \tag{2.36}$$

or, in matricial form,

$$\begin{bmatrix} \dfrac{\partial N_i}{\partial \xi} \\ \dfrac{\partial N_i}{\partial \eta} \end{bmatrix} = \begin{bmatrix} \dfrac{\partial x}{\partial \xi} & \dfrac{\partial y}{\partial \xi} \\ \dfrac{\partial x}{\partial \eta} & \dfrac{\partial y}{\partial \eta} \end{bmatrix} \begin{bmatrix} \dfrac{\partial N_i}{\partial x} \\ \dfrac{\partial N_i}{\partial y} \end{bmatrix} . \tag{2.37}$$

The first matrix on the right-hand side of Equation 2.37 is called the Jacobian matrix, denoted as $\mathbf{J}$. In the isoparametric formulation of finite elements, the shape functions that approximate the solutions within the element are the same that execute the coordinate transformation between the local and global scales. Because of that, the Jacobian can be found explicitly in terms of the local coordinates, as long as the nodes coordinates in the global reference system (x_i, y_i) are known [48]. The Jacobian becomes:

$$\mathbf{J} = \begin{bmatrix} \sum_{i=1}^{4} \dfrac{\partial N_i}{\partial \xi} x_i & \sum_{i=1}^{4} \dfrac{\partial N_i}{\partial \xi} y_i \\ \sum_{i=1}^{4} \dfrac{\partial N_i}{\partial \eta} x_i & \sum_{i=1}^{4} \dfrac{\partial N_i}{\partial \eta} y_i \end{bmatrix} = \begin{bmatrix} \dfrac{\partial N_1}{\partial \xi} & \dfrac{\partial N_2}{\partial \xi} & \dfrac{\partial N_3}{\partial \xi} & \dfrac{\partial N_4}{\partial \xi} \\ \dfrac{\partial N_1}{\partial \eta} & \dfrac{\partial N_2}{\partial \eta} & \dfrac{\partial N_3}{\partial \eta} & \dfrac{\partial N_4}{\partial \eta} \end{bmatrix} \begin{bmatrix} x_1 & y_1 \\ x_2 & y_2 \\ x_3 & y_3 \\ x_4 & y_4 \end{bmatrix} \quad . \tag{2.38}$$

Equation 2.37 indicates that to determine the partial derivatives of the shape functions

with respect to the global coordinates, the inverse of $\mathbf{J}$ is applied:

$$\begin{bmatrix} \frac{\partial N_i}{\partial x} \\ \frac{\partial N_i}{\partial y} \end{bmatrix} = \mathbf{J}^{-1} \begin{bmatrix} \frac{\partial N_i}{\partial \xi} \\ \frac{\partial N_i}{\partial \eta} \end{bmatrix} \quad . \tag{2.39}$$

The $\mathbf{B}$ matrix can then be written explicitly with respect to the local coordinates. Next, the limits of integration of Equation 2.29 must be adjusted, as well as the integrand must be multiplied by the determinant of $\mathbf{J}$ because of the transformation of coordinates in element e:

$$\mathbf{k}_e = \int_{V_e} \mathbf{B}_e^T \mathbf{C}_e \mathbf{B}_e \det(\mathbf{J}_e) \ \ dV_e \quad . \tag{2.40}$$

In the most traditional formulations, the full stiffness matrix $\mathbf{K}$ and the full load vector $\mathbf{F}$ are assembled. They are created according to the global node enumeration. It is important to note that, conventionally, the local node enumeration within the elements begins with the lowest left-most node, following a counter-clockwise order, but the global enumeration of DOF at the full structure is based on the ordering of the elements, which is stored in an auxiliary data structure. Equation 2.29 than takes the form:

$$\mathbf{K}\mathbf{d} = \mathbf{F} \quad . \tag{2.41}$$

It is worth noting that the elements are only connected to their close neighbors. That is to say, each node is only shared by a few of the many elements a structure can have, making $\mathbf{K}$ take the form of a sparse positive definite matrix.

Further details on the FEM can be found in the vast literature, including the works of Zienkiewicz and Taylor [48], Fish and Belytschko [11], Reddy [32], and Zohdi [49], to name a few.

2.3 Homogenization Theory

Even though most structural materials are considered homogeneous for design simplification purposes, they are generally composed of several constituents at the microscale. There are cases in which the distinct nature of the constituents is preponderant in determining the response of the material, such as in long-term loadings on viscoelastic problems. In these circumstances, the microstructural arrangement of the heterogeneous material must be taken in account to define the homogenized property. Homogenization is, hence,

the procedure of finding the properties of a theoretical homogeneous material that is analogue and equivalent to the real heterogeneous one.

A homogenization problem has at least two well-separated scales: the local (or micro), in which the heterogeneities are distinguishable, and the global (or macro), in which the material is perceived as a homogenous body [23], not necessarily isotropic [14]. For this reason, a homogenization problem is multiscale in essence, as it respects the principle of separation of scales [12], which states that the global scale is much bigger than the local scale.

The homogenization of heterogeneous viscoelastic materials can be executed using the mean-field technique, the simplest homogenization procedure [15]. The mean-field homogenization is done by considering the mean value of a field within each constituent at the microscale as the homogenized value of that field at the macroscale. Given a domain Ω, with a field ϕ described in it, its homogenized value $\langle\phi\rangle$ is given by:

$$\langle\phi\rangle = \frac{1}{|\Omega|}\int_{\Omega} \phi \, d\Omega \quad , \tag{2.42}$$

where $|\Omega|$ is the size of Ω. The bracket notation $\langle\blacksquare\rangle$ denotes the average of $\blacksquare$. This relation can be manipulated to get an homogenized material property from the properties of the constituents.

In Equation 2.42, Ω corresponds to a portion of the microstructural configuration called Representative Volume Element (RVE), which contains enough information to represent the homogenized material, or synthesizes a unitary periodic cell of a mathematically infinite periodic material [30]. The RVE is the model employed in the FEM analysis.

Figure 2.6 illustrates the translation between scales. A macro kinematic quantity is transferred to the microscale to create a Boundary Value Problem (BVP) on an RVE. As the RVE is considered a single periodic cell of an infinite material, Periodic Boundary Conditions (PBC) are applied to its edges. These conditions simulate the infinite repetitions of the RVE in all directions. Once the problem is solved, the corresponding dynamic quantity is transferred back to the macroscale using Equation 2.42. In a linear elastic problem, a strain field from the macroscale is applied to the microscale, resulting in a homogenized stress field.

Although viscoelasticy is a phenomenon only observable at different instants in time, for practical purposes, as explained in Chapter 3, the homogenization framework is described here for a static analysis in the linear elastic regime. In that case, the relation

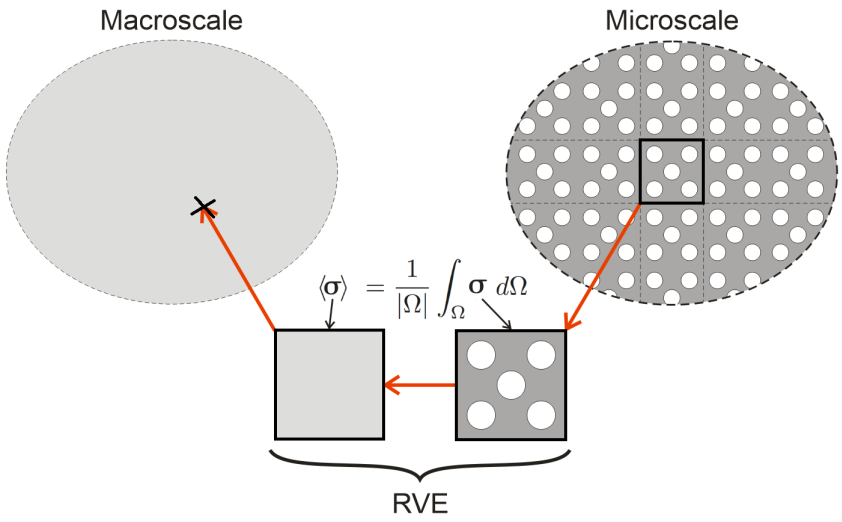

Figure 2.6: Transport of information between the micro and macro scales in the homogenization process.

between applied strain and stress state is given by the generalized Hooke's law [21]:

$$\sigma_{ij} = E_{ijkl}\varepsilon_{kl} \quad , \tag{2.43}$$

where σ_{ij} is the stress tensor, ε_{kl} is the strain tensor, and E_{ijkl} is the constitutive tensor that contains the material elastic properties. Due to symmetries within these three tensors, Equation 2.43 can be written in a matricial form called Voigt notation, and it reads:

$$\begin{bmatrix} \sigma_{11} \\ \sigma_{22} \\ \sigma_{33} \\ \sigma_{23} \\ \sigma_{13} \\ \sigma_{12} \end{bmatrix} = \begin{bmatrix} E_{1111} & E_{1122} & E_{1133} & E_{1123} & E_{1113} & E_{1112} \\ E_{2211} & E_{2222} & E_{2233} & E_{2223} & E_{2213} & E_{2212} \\ E_{3311} & E_{3322} & E_{3333} & E_{3323} & E_{3313} & E_{3312} \\ E_{2311} & E_{2322} & E_{2333} & E_{2323} & E_{2313} & E_{2312} \\ E_{1311} & E_{1322} & E_{1333} & E_{1323} & E_{1313} & E_{1312} \\ E_{1211} & E_{1222} & E_{1233} & E_{1223} & E_{1213} & E_{1212} \end{bmatrix} \begin{bmatrix} \varepsilon_{11} \\ \varepsilon_{22} \\ \varepsilon_{33} \\ \gamma_{23} \\ \gamma_{13} \\ \gamma_{12} \end{bmatrix} \implies \boldsymbol{\sigma} = \mathbf{C}\boldsymbol{\varepsilon} \quad . \tag{2.44}$$

where $\mathbf{C}$ is the matricial form of the constitutive tensor $\boldsymbol{E}$, and $\gamma_{kl} = 2\varepsilon_{kl}$, generally called engineering shear strain coefficients.

As indicated by Equations 2.42 and 2.44, the stress state at the macroscale $\langle \boldsymbol{\sigma} \rangle$ is equal to the inner product of the homogenized constitutive matrix $\mathbf{C}^h$ and the strain state at the macroscale $\langle \boldsymbol{\varepsilon} \rangle$. Hence, to find $\mathbf{C}^h$, one only needs to find $\langle \boldsymbol{\sigma} \rangle$ for a given $\langle \boldsymbol{\varepsilon} \rangle$. The simplest way of doing so is performing the numerical homogenization six times, because $\mathbf{C}^h$ is a 6×6 matrix. The whole homogenization process is executed by applying a different unitary strain in each entry of $\langle \boldsymbol{\varepsilon} \rangle$ at a time, that is, three analyses are run

with the application of a normal strain, and three others applying a shear strain. Each one promptly gives the corresponding column of $\mathbf{C}^h$ in $\langle\boldsymbol{\sigma}\rangle$, as shown in the example of Equation 2.45.

$$\begin{bmatrix}\langle\sigma\rangle_{11}\\ \langle\sigma\rangle_{22}\\ \langle\sigma\rangle_{33}\\ \langle\sigma\rangle_{23}\\ \langle\sigma\rangle_{13}\\ \langle\sigma\rangle_{12}\end{bmatrix} = \begin{bmatrix} \mathrm{C}^h_{11} & \mathrm{C}^h_{12} & \mathrm{C}^h_{13} & \mathrm{C}^h_{14} & \mathrm{C}^h_{15} & \mathrm{C}^h_{16}\\ \mathrm{C}^h_{21} & \mathrm{C}^h_{22} & \mathrm{C}^h_{23} & \mathrm{C}^h_{24} & \mathrm{C}^h_{25} & \mathrm{C}^h_{26}\\ \mathrm{C}^h_{31} & \mathrm{C}^h_{32} & \mathrm{C}^h_{33} & \mathrm{C}^h_{34} & \mathrm{C}^h_{35} & \mathrm{C}^h_{36}\\ \mathrm{C}^h_{41} & \mathrm{C}^h_{42} & \mathrm{C}^h_{43} & \mathrm{C}^h_{44} & \mathrm{C}^h_{45} & \mathrm{C}^h_{46}\\ \mathrm{C}^h_{51} & \mathrm{C}^h_{52} & \mathrm{C}^h_{53} & \mathrm{C}^h_{54} & \mathrm{C}^h_{55} & \mathrm{C}^h_{56}\\ \mathrm{C}^h_{61} & \mathrm{C}^h_{62} & \mathrm{C}^h_{63} & \mathrm{C}^h_{64} & \mathrm{C}^h_{65} & \mathrm{C}^h_{66} \end{bmatrix} \begin{bmatrix}1\\0\\0\\0\\0\\0\end{bmatrix} \implies \begin{bmatrix}\mathrm{C}^h_{11}\\ \mathrm{C}^h_{21}\\ \mathrm{C}^h_{31}\\ \mathrm{C}^h_{41}\\ \mathrm{C}^h_{51}\\ \mathrm{C}^h_{61}\end{bmatrix} = \begin{bmatrix}\langle\sigma\rangle_{11}\\ \langle\sigma\rangle_{22}\\ \langle\sigma\rangle_{33}\\ \langle\sigma\rangle_{23}\\ \langle\sigma\rangle_{13}\\ \langle\sigma\rangle_{12}\end{bmatrix} . \tag{2.45}$$

Figure 2.7 illustrates the proposed perturbations applied to a 2-D problem, for conciseness. The principle is extensible to 3-D.

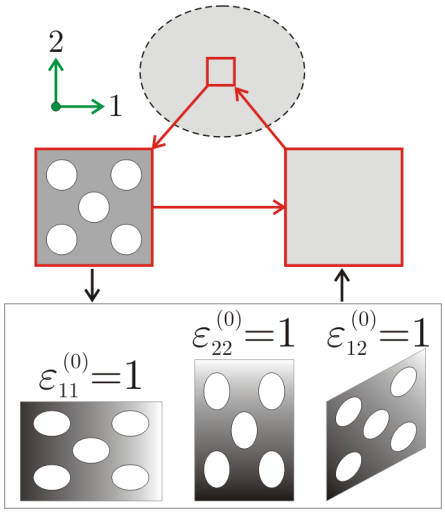

Figure 2.7: Unitary strains applied in the process of a 2D homogenization.

The principle of separation of scales implies that the whole RVE is considered not more than a point at the macroscale. As a consequence, the strain state at a single point at the macroscale is transported to the microscale as an action over the entire RVE domain. Because of the separation of scales, the definition of a strain, that is a differentiation of the displacement field, can be perceived as a difference, as demonstrated in Equation 2.46:

$$\varepsilon_{ij} = \frac{1}{2}\left(\frac{\partial u_i}{\partial x_j} + \frac{\partial u_j}{\partial x_i}\right) \implies \varepsilon_{ij} = \frac{1}{2}\left(\frac{\Delta u_i}{\Delta x_j} + \frac{\Delta u_j}{\Delta x_i}\right) , \tag{2.46}$$

where $\boldsymbol{u}$ is the displacement field and $\boldsymbol{x}$ is the system of reference.

Let the RVE be a square of side L. As $\langle\boldsymbol{\varepsilon}\rangle$ is applied to the entire domain, the differences demonstrated in Equation 2.46 are defined for the opposite sides of the RVE.

Hence, considering the origin of the reference system at the bottom left corner of the RVE, for the specific case of Equation 2.45:

$$\langle \varepsilon \rangle_1 = 1 = \frac{1}{2}\left(\frac{u_L - u_0}{x_L - x_0} + \frac{u_L - u_0}{x_L - x_0}\right) \implies 1 = \frac{\Delta u}{L} \implies \Delta u = L \quad . \tag{2.47}$$

Equation 2.47 indicates that the BVP on the RVE is solved by obligating the difference of displacements between edges to be equal to the side of the square RVE. In this work, this difference is attained by enforcing the displacements at the FEs to follow a linear function of the coordinates throughout the entire domain. Once the BVP is solved using FEM, the displacements enforced by means of $\langle \boldsymbol{\varepsilon} \rangle$ must be subtracted from the final the solution in order to calculate the homogenized stress matrix with Equation 2.44:

$$\langle \boldsymbol{\sigma} \rangle = \frac{1}{|\Omega|} \int_{\Omega} \mathbf{C}^h \left(\boldsymbol{\varepsilon}^{(0)} - \boldsymbol{\varepsilon} \right) \, d\Omega \ , \tag{2.48}$$

where $\boldsymbol{\varepsilon}^{(0)}$ represents the macro strain field applied to the domain, and $\boldsymbol{\varepsilon}$ is the strain field calculated from the governing equations through the BVP at the microscale.

3 The Finite Element Solver

The low-memory matrix-free approach has the drawback of demanding a greater processing time in addition to the great increase in the capacity to solve large-scale problems. In this work, the Preconditioned Conjugate Gradient method (PCG) is employed to solve the systems of equations. The PCG is an iterative numerical solver that gives a reasonably accurate solution (given a reasonable tolerance) in relatively few steps. More information on the PCG method can be found within a didactic approach in [40].

The Finite Element Method (FEM) transforms partial differential equations into algebraic ones. The method requires discretization of the domain, what can be a tiresome and time-demanding task depending on the model. There are, however, techniques available to optimize the procedure. For instance, in image-based approaches to a FEM problem, voxel-based meshes are created easily and can be extremely efficient.

3.1 Model discretization

Voxels are the smallest pieces of detail attainable from images. So, when creating a FE mesh from an image file, considering each one of them as individual finite elements is the most intuitive thought. This way, all the details of the image are inescapably included in the model. Besides, all voxels have the same dimensions, and are characterized each by a color value within a defined range (for 8-bit images, for example, the value goes from 0 to 255). These values can be interpreted as keys that identify materials. With this approach, there is no need to spend any further effort in mesh generation. The image itself is already the structured mesh, because the image file, as nothing more than an array, contains an ordering of all the voxels within it. Consequently, ordering the elements is another task avoided in image-based approaches to FEM problems. In short, all elements are equally hexahedral, connected, ordered, and associated to a single material key.

This procedure also allows a great economy in memory allocation. It is possible to avoid storing the model's full stiffness matrix by employing an assembly-free strategy. A

single small local stiffness matrix is calculated for each material, and the coefficients of the system of equations are computed on-the-fly through loops that sweep the entire domain at each step of the iterative solver. For example, considering a 3D cubical image with n voxels in each direction, 3 Degrees of Freedom (DOF) per node, discretized in 8-node hexahedral elements. Instead of storing a $3n^3 \times 3n^3$ sparse stiffness matrix, it would only be necessary to store a n^3 array for a material map (the image itself), and a $(n+1)^3$ array to map the DOF within the model. This reduction makes possible the analysis of models with hundreds of millions of DOF in not so sofisticated machines. Furthermore, the strategy is extremely versatile to be applied to all sorts of composites, because, using simple 8-bit images, heterogeneous materials with up to 256 different constituents can be represented.

3.2 Periodic boundary conditions

The problems tackled with the scheme proposed here involve models that are considered to be Representative Volume Elements (RVEs) of a theoretical infinite periodic medium, so the Periodic Boundary Conditions (PBC) are enforced on the DOF numbering scheme. This is done by matching the indexes of nodes on opposite borders of the mesh, as illustrated in Figure 3.1.

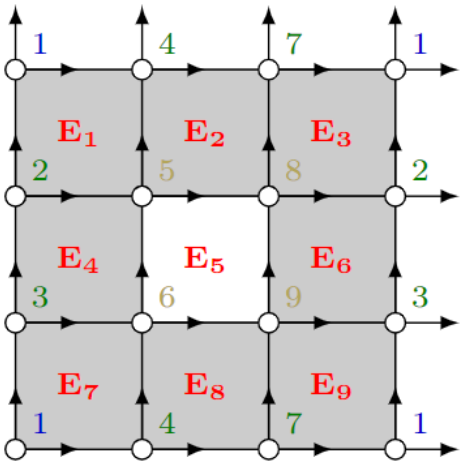

Figure 3.1: 2-D example of enforcement of PBC to represent an infinite periodic material.

The imposition of PBC assumes that the RVE is a periodic cell that repeats itself infinitely in all directions. For actual periodic materials it gives the consistent solution of the problem, but in reality, most materials are highly diverse at the microscale. For this reason, the size of the RVE must not only be much smaller than the actual size of the material application at the macroscale, in order to account for the principle of separation

of scales, but also must be large enough to be representative of the actual equivalent homogenized material. The definition of the RVE size is object of study in many areas [26, 29, 3], and its size definition varies according to the studied material. In general, the most simple procedure in RVE size definition is the property convergence. In short words, RVEs of growing sizes are tested and the solutions are compared. When the results start to converge to the same value, the RVE size is defined for that material [26]. That is the procedure adopted in this work for the real materials.

3.3 Inputs and outputs

In regard of Equation 2.17, it is clear that the value of E of any viscoelastic material can be found at any instant t if the Prony series parameters are known. That value can thus be incorporated to Equation 2.29 to find $\mathbf{k}_e$ at the same instant t, and use it to perform an elastic homogenization at that instant. With a fine enough discretization of a period of time, the whole homogenized relaxation master curve can be created. Hence, besides the images, the other inputs necessary to perform the analyses with the proposed scheme are the material properties, which are associated to voxel colors, and a discretized time span that is covered by the analysis.

In the code developed for this work, the time domain is determined by an initial instant, a final instant, and a method for discretizing the gap between them. Due to the exponential nature of the generalized models, as discussed in Chapter 2, the time discretization normally follows a division by decades. Needless to say, the time gap used covered by the analysis must contain the interval in which the variation of the relaxation modulus occurs.

In the proposed scheme, all the constituents can be potentially viscoelastic, either isotropic or anisotropic. Specifically in the present work, only isotropic behavior is considered. For elastic materials, the required properties are the Young's modulus and the Poisson's ratio. For viscoelastic materials, it must be provided the Poisson's ratio and the Prony series' parameters for the relaxation modulus (E^i, τ^i and E^∞ in Equation 2.17).

The analyses output the Prony series parameters that adjust the obtained master curve. This adjustment can be done through several methods. The most traditional one is the collocation method, proposed by Schapery [34], consisting in the solution of a simple system of equations. It is worth noting that it is also applicable for interconverting between the viscoelastic properties, such as creep compliance and complex modulus [28].

In the collocation method, some of the known points of the master curve are chosen to calculate the parameters. In order to use all of the known points, the least squares method for curve adjustment was employed in this work. With the least squares method it is possible to compute as many Prony series parameters as desired.

Due to the nature of the exponent function, the value of each Prony series term varies greatly within only two orders of magnitude in time. As a consequence, the optimum way to capture the nuance of the homogenized master curve is defining the Prony series two terms shorter than the number of decades in the period covered by the analysis, provided that at both the initial and final instants the curve is stabilized. Fewer terms may closely describe the curve, but more of them will never increase precision.

3.4 Algorithm

The property computed with the scheme introduced in this work is the relaxation moduli of the material using the generalized Maxwell model. However, with few modifications, the creep compliance can be attained too, using whichever model. The general scheme for the program developed is described in Algorithm 1.

Algorithm 1 Image-based numerical homogenization of viscoelastic properties

1: **Input:** Image, material properties, numerical tolerance, initial instant, final instant, time discretization.
2: **Output:** Prony series parameters for the homogenized relaxation moduli.
3: Generate DOF map.
4: Generate time steps: `time`.
5: Initialize $\mathbf{C}^h$ for each time step.
6: **for** t in `time` **do**
7: Compute local matrices for each material.
8: **for** i in (1,...,dim$_{\mathbf{C}^h}$) **do**
9: Assemble force vector $\mathbf{f}$ (macro- to microscale).
10: Solve system (PCG): $\mathbf{Kd} = \mathbf{F}$ (microscale).
11: Compute average stress field (microscale).
12: Update column i of $\mathbf{C}^h(t)$ (micro- to macroscale).
13: **end for**
14: **end for**
15: Compute parameters of the Prony series for the relaxation moduli based on all $\mathbf{C}^h$.

Once the homogenized relaxation tensor $\mathbf{C}^h$ is calculated for all discrete instants, the engineering moduli E_1, E_2, and E_3 (and whichever other properties are desired) are extracted for each discrete instant, by considering $\mathbf{C}^h$ the constitutive matrix of an

orthotropic material. Different homogenized Prony series parameters are then calculated for each orthotropic relaxation modulus computed from $\mathbf{C}^h$. Algorithm 1 is completely versatile, and is the basic procedure for performing the homogenization of either the relaxation moduli as well or the creep compliance directly in the time domain, in 2-D or 3-D cases.

Following the procedure established in this chapter, the viscoelastic properties of any heterogeneous material can be characterized. An important observation is that the methodology is perfectly capable of handling and perceiving anisotropy at the macroscale. For summarizing the procedure, the flowchart in Figure 3.2 illustrates the pipeline of procedures described in Algorithm 1.

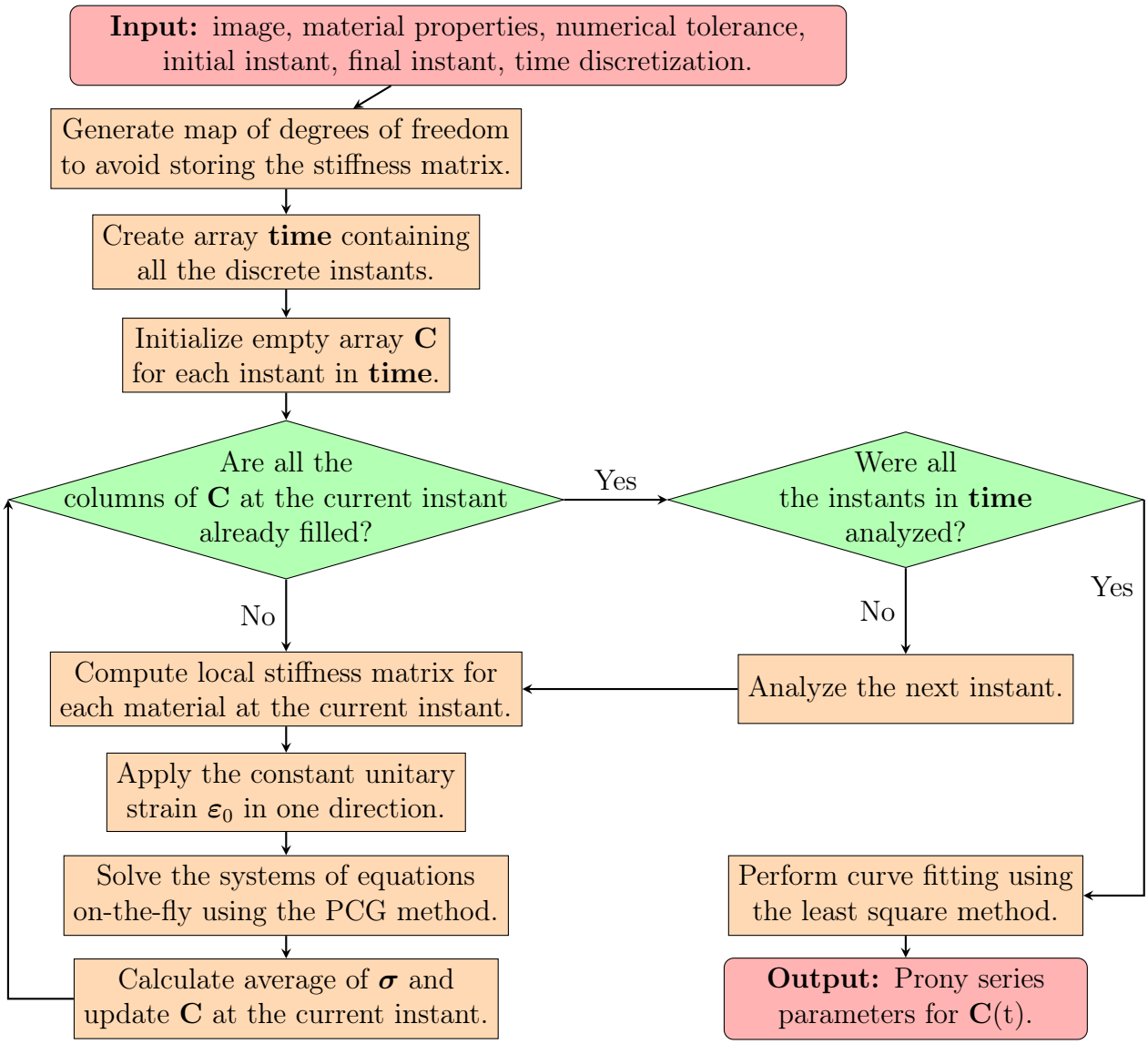

Figure 3.2: Flowchart of the proposed scheme.

An implementation of Algorithm 1 in Julia language is available here. The codes

presented can solve 2-D and 3-D problems, and the input files used to study the examples in Chapter 4 are made available too.

4 Verification

Although much has been discussed on viscoelastic homogenization in recent years, it is difficult to find solutions for numerical examples solved in the time domain in the literature for comparison purposes. Thus, the solution of two problems with synthetic models and different levels of complexity are presented to demonstrate the effectiveness of the proposed scheme. In the first problem, homogenization studies were conducted on 2-D models containing a circular elastic inclusion embedded in a viscoelastic matrix. Next, the homogenization of a 3-D synthetic composite consisting of a viscoelastic matrix with cross-layered cylindrical elastic inclusions was performed.

4.1 Verification in 2-D: periodic circular elastic inclusions embedded in a linear viscoelastic matrix

Yi et al. [44] present the numerical homogenization of relaxation moduli of four 2-D plane stress models consisting of an elastic circular inclusion embedded in a viscoelastic matrix. Each model contains a different volume fraction of inclusion, those being 10%, 30%, 50%, and 70% of the total cell area. The homogenization is performed at the frequency domain using the Laplace-Carson transform, and the Prony series parameters are not calculated. The results provided are the master curves of the first element of the relaxation matrix for each volume fraction. The utilized material properties are arbitrary, and are described in Tables 4.1 and 4.2.

Elastic inclusions	
ν	0.21
E [Pa]	20.0
Viscoelastic matrix	
ν	0.38
E^{∞} [Pa]	3.0

Table 4.1: Material data for the 2-D models.

i	τ^i [s]	E^i [Pa]
1	10	10
2	1	7

Table 4.2: Prony series parameters for the relaxation modulus of the viscoelastic matrix of Table 4.1.

To reproduce the analyses, four square 8-bit images measuring 1000 pixels in each side were created to serve as input for the analysis. The centered circular inclusion radius in pixels at each image was 178, 309, 399, and 472, making the inclusion volume fractions approximately the same as the reference. With two Degrees of Freedom (DOF) per node and Periodic Boundary Conditions (PBC) applied, these images generate models with 1e6 DOF. Using double precision and the Preconditioned Conjugate Gradient (PCG) method, the memory necessary to analyze these models with the proposed scheme revolves around 90 MB at the bottleneck, while solely storing the whole stiffness matrix as a band symmetric sparse matrix in CSR format would need around 140 MB. In 3-D analyses the memory savings are even more expressive, as will be shown in the next examples.

The models are presented in figure 4.1.

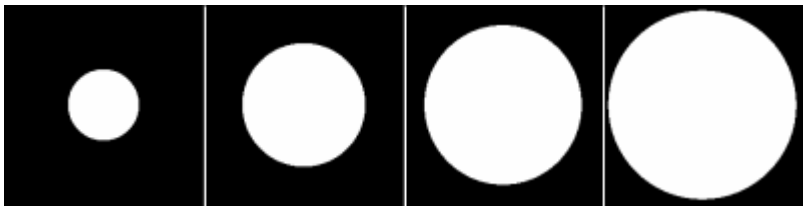

Figure 4.1: Models with 10%, 30%, 50%, and 70% of elastic inclusion volume fraction.

Figure 4.2 shows the good match between the results foundT for the master curves of the first element of the relaxation matrix for each volume fraction by Yi et al. [44] and the proposed scheme. At all calculated instants the relative difference between the results stayed below 10% for all the inclusion volume fractions. The proposed scheme represents well the curve expected.

4.2 Verification in 3-D: Cross-layered inclusions embedded in a linear viscoelastic matrix

The second problem analyzed is a 3-D model of a composite made of cross-layered elastic glass fibers embedded in a viscoelastic epoxy resin, proposed by Naik et al.[27] The material data for the epoxy matrix and the glass fibers are described in Tables 4.3 and 4.4.

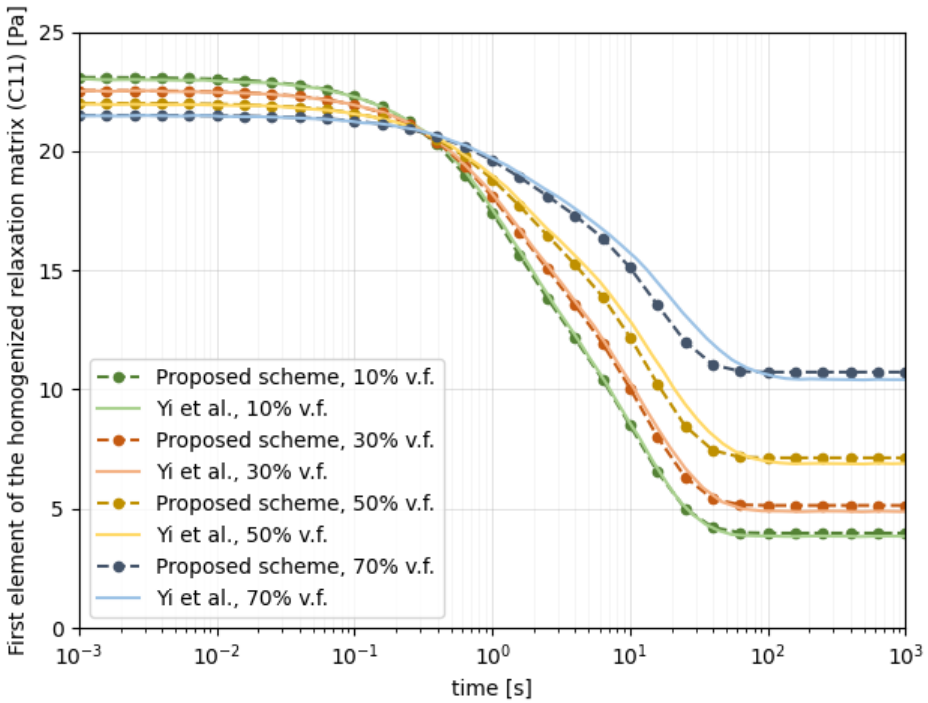

Figure 4.2: Comparison of results obtained by Yi et al. [44] and by the proposed scheme for the 2D plane stress model.

Elastic inclusions	
ν	0.3
E [MPa]	80000.0
Viscoelastic matrix	
ν	0.4
E^{∞} [MPa]	707.9

Table 4.3: Material data for the cross-layered models.

Four stacks of 100 slices representing the cross-layered periodic material were created. Each slice is a 100 × 200 pixels image that comprises the fibers in both directions. Figure 4.3 illustrates the studied periodic unit cells. With three DOF per node and PBC applied, these images generate models with 6e6 DOF. Using double precision and the PCG method, the memory necessary to analyze the models with the proposed scheme revolves around 260 MB at the bottleneck, while solely storing the whole stiffness matrix as a band symmetric sparse matrix in CSR format would need around 3144 MB. These are rather small models, and the amount of memory space saved already shows that much bigger problems can be solved with the proposed scheme.

Figures 4.4, 4.5, and 4.6 show the master curves of the relaxation moduli found for each

i	τ^i [s]	E^i [MPa]
1	1.01e−09	166.5
2	1.01e−08	336.5
3	1.01e−07	824.4
4	1.01e−06	1014
5	1.01e−05	1696
6	1.01e−04	1941
7	1.01e−03	2395
8	1.01e−02	2261
9	1.01e−01	1099
10	1.01e+00	460.0
11	1.01e+01	158.7
12	1.01e+02	127.2

Table 4.4: Prony series parameters for the relaxation modulus of the viscoelastic matrix of Table 4.3.

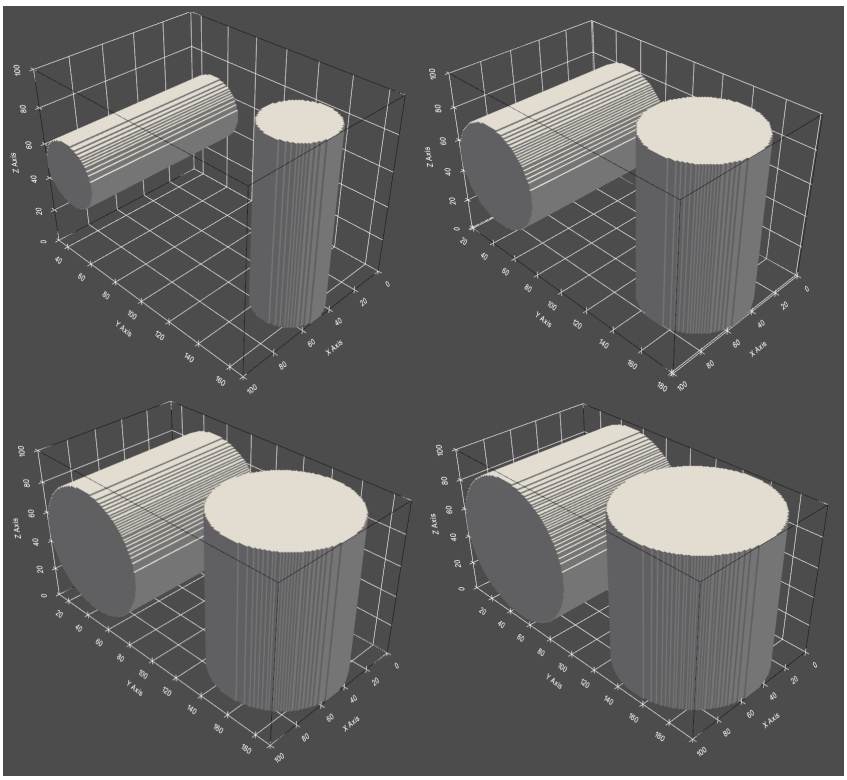

Figure 4.3: Cross-layered fiber models. The fibers are elastic, embedded in a viscoelastic matrix. The fiber inclusions represent 10% (top left), 30% (top right), 50% (bottom left), or 70% (bottom right) of the total volume.

model in directions x_1, x_2, x_3, respectively. For comparison purposes, the master curve of the epoxy relaxation modulus is also plotted. The scheme successfully captured not only the change in stiffness due to the different volumes of elastic inclusions, but also the transversely isotropic behavior, which is a consequence of the orientation of the cylindrical inclusions. In the direction normal to the two layers of fibers (that is, normal to the axes

of the inclusions in the RVE) the stiffness relaxation was much more pronounced than in the other two. Furthermore, as the volume of elastic inclusions grows, the viscoelastic behavior is less expressive. For all volume fractions, the composite stiffness was higher than the matrix stiffness, as expected.

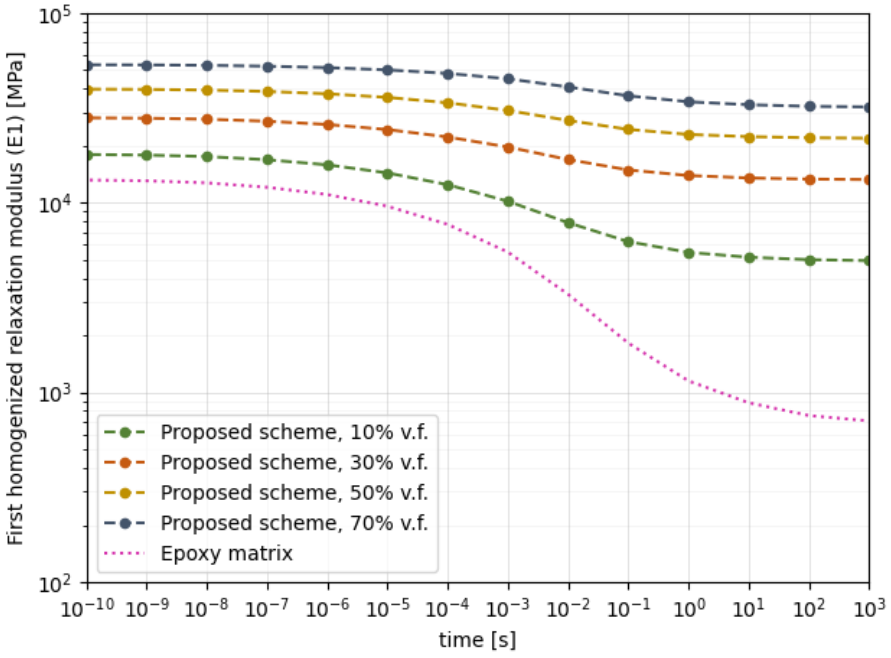

Figure 4.4: Relaxation modulus, E_1, for the cross-layered composite.

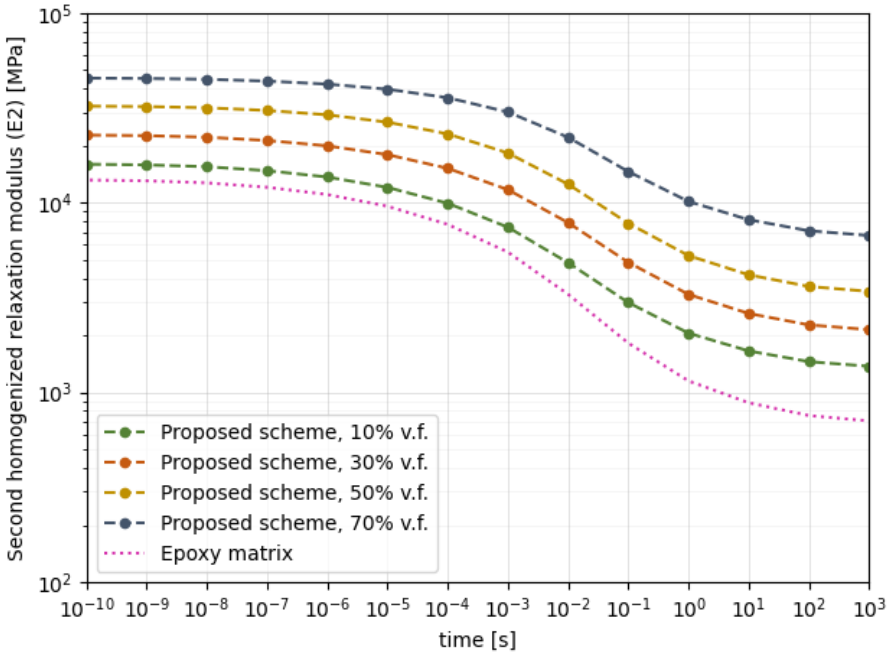

Figure 4.5: Relaxation modulus, E_2, for the cross-layered composite.

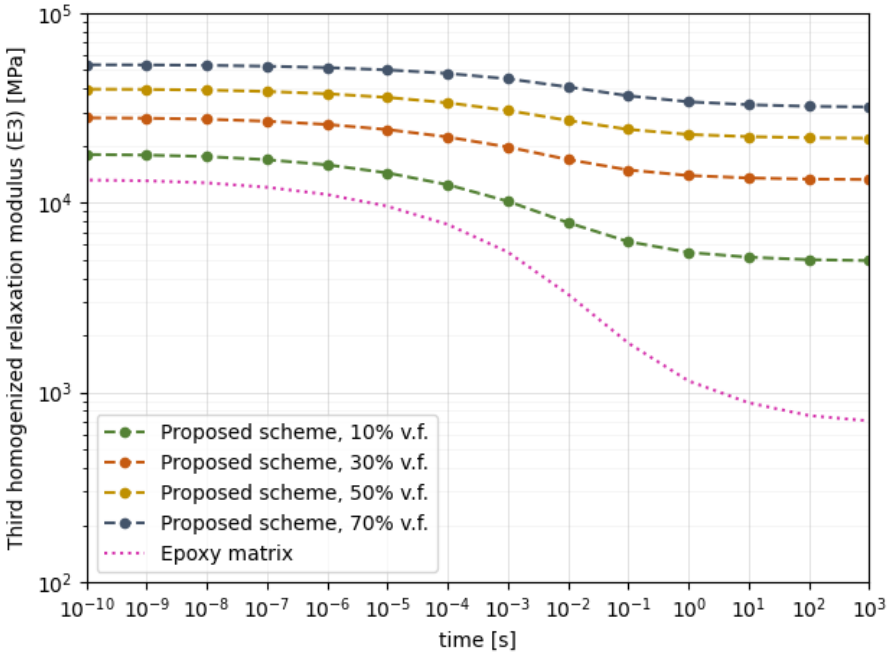

Figure 4.6: Relaxation modulus, E_3, for the cross-layered composite.

The Prony series parameters of the master curves were determined with an optimization problem using the least squares method. As the stiffness and relaxation time of each Prony series term have physical meaning, they must be non-negative. Because of that, the L-BFGS method described in [18] was employed.

First, the desired number of Prony series terms must be determined. Following the reasons described in Chapter 3, the time span covered by the relaxation times was defined in two orders of magnitude fewer than the covered by the known points. The division followed one term per decade, resulting in 12 terms allocated in the middle of the time period. The relaxation times were fixed at the first integer power of 10 in each decade. Next, the long-term E^{∞} parameters were determined by considering the master curves stabilized at their last known point. At last, the L-BFGS bounding box for the remaining coefficients was defined with the bottom limit of 1% of E^{∞}, and the upper limit of $100 \times E^{0}$. The results for the three normal relaxation moduli of each model are presented in Tables 4.5 and 4.6. It is worth noting the parameters are equivalent for the directions in which the elastic cylinders are aligned, as expected.

		E^i [MPa]			
i	τ^i [s]	10%	30%	50%	70%
1	1.0e−9	325.4	325.0	253.8	319.6
2	1.0e−8	103.4	285.2	237.6	319.6
3	1.0e−7	948.7	631.7	828.5	421.5
4	1.0e−6	1017	1422	1124	1111
5	1.0e−5	1657	1444	1713	1428
6	1.0e−4	1940	2263	2541	2318
7	1.0e−3	2587	2892	3156	3219
8	1.0e−2	2271	2790	3972	5020
9	1.0e−1	1379	1676	2253	3959
10	1.0e+0	475.6	640.3	1099	1914
11	1.0e+1	155.8	266.5	386.7	802.9
12	1.0e+2	194.7	205.6	272.3	630.7
∞	-	4951	13240	21870	31960

Table 4.5: Prony series parameters for E_1 and E_3 of the cross-layered inclusions model.

		E^i [MPa]			
i	τ^i [s]	10%	30%	50%	70%
1	1.0e−9	320.7	390.2	436.8	441.4
2	1.0e−8	100.0	125.1	123.3	257.4
3	1.0e−7	1112	1335	1621	1170
4	1.0e−6	1080	1219	1307	1763
5	1.0e−5	1717	2335	3084	2691
6	1.0e−4	2289	2721	3374	4158
7	1.0e−3	2692	4054	5531	6316
8	1.0e−2	2709	3982	6289	9239
9	1.0e−1	1533	2570	4119	7028
10	1.0e+0	595.1	1149	1870	3256
11	1.0e+1	278.3	368.7	557.3	1347
12	1.0e+2	207.7	381.0	636.3	1034
∞	-	1374	2142	3409	6717

Table 4.6: Prony series parameters for E_2 of the cross-layered inclusions model.

5 Applications

Two problems with real materials are presented in this chapter to exemplify the possible applications of the proposed scheme. First, X-ray micro-CT images of a fiber-reinforced polymer (FRP) composite were employed to analyze a real sample. Next, three mixtures of asphaltic concrete were homogenized and the numerical solutions were compared to experimental results.

5.1 Fiber-reinforced polymer composite

The first case studied with a real material is the application of the proposed scheme to X-ray micro-CT scans of a composite made of a viscoelastic epoxy matrix with unidirectional glass fiber inclusions. The digital sample used in this work was made available by Mehdikhani et al. [22] The image stack characteristics are shown in Table 5.1.

Rows	933
Columns	384
Slices	411
Voxel size	1.1μm
Volume	0.2 mm^3

Table 5.1: Micro-CT stack characteristics.

In spite of the high quality of the images, a segmentation of the stack in two phases was performed to specify an 8-bit tone to each material. Small defects arising from the micro-CT acquisition were adjusted in the segmentation. Fiber inclusions appearing to be hollow were filled, and the fibers that were apparently bonded were separated using watershed techniques for image treatment. The open-source Fiji ImageJ software [36] was used to carry out the segmentation. Figure 5.1 shows some slices of the original image, while Figure 5.2 portrays the segmentation applied to those slices. In Figure 5.3, a portion of the segmented image with $364 \times 364 \times 364$ voxels is presented. This representation makes clear the unidirectional orientation of the fibers.

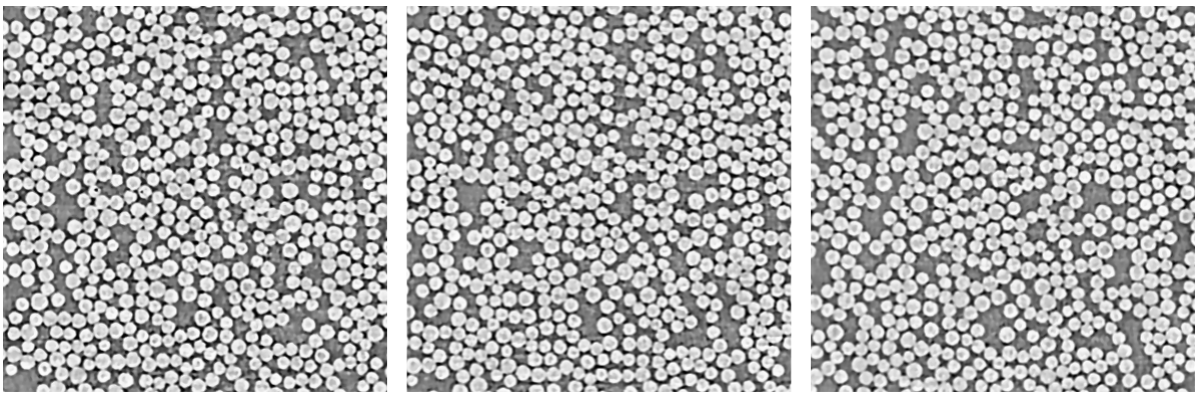

Figure 5.1: Parts of slices 0, 200, and 400 of the micro-CT scans prior to segmentation.

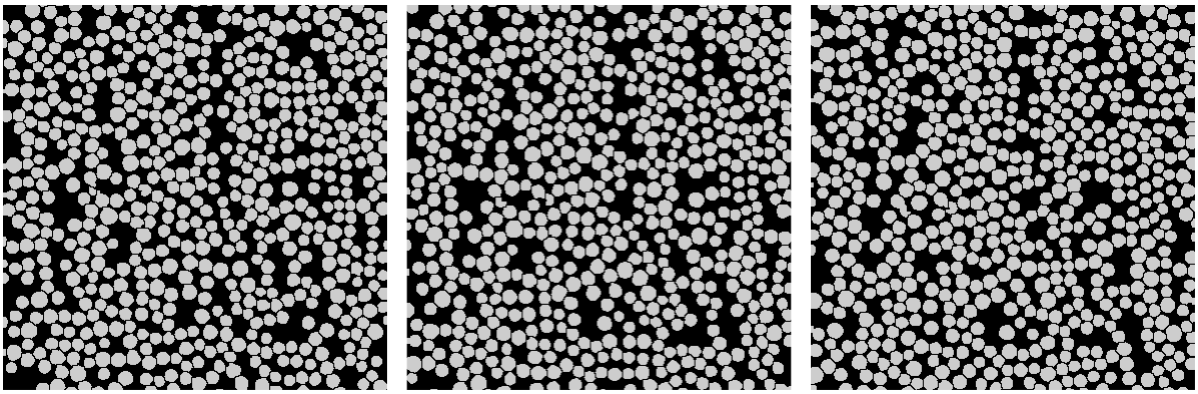

Figure 5.2: Parts of slices 0, 200, and 400 after segmentation.

In opposition to the previous examples wherein the models are naturally periodic cells, the micro-CT images are not periodic, making additional steps for the characterization necessary. Although a small volume containing the microscale arrangement of a material can single-handedly present characteristics that are observable at the macroscale, it may not be representative due to its size. To assure that the properties found with a microstructural model are the same as the homogenized material, a convergence analysis must be performed, as described in Chapter 3. Material subvolumes of different sizes, henceforth called Regions of Interest (ROI), must be homogenized, and as the value of the desired property stabilizes, the Representative Volume Element (RVE) is determined and the homogenized property is defined.

For the characterization of this FRP, twelve cubical ROIs were defined across three different regions of the stack to investigate the sample homogeneity. In each region, a starting point was determined and four ROIs were extracted spanning from them. The first point defined was at $(0, 0, 0)$, and the ROIs grew along the direction of the axes. That region was called front region. The second point was at $(\text{end}, \text{end}, \text{end})$, with the ROIs growing on the inverse direction of the axes. That region was called back region.

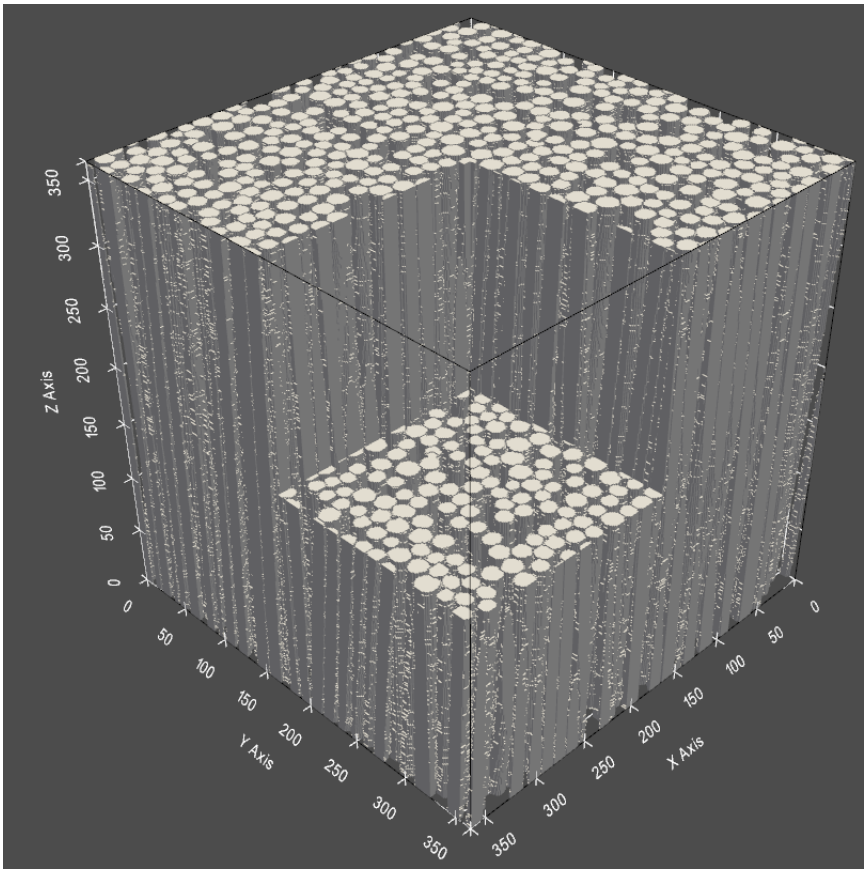

Figure 5.3: 3D rendering of the elastic fiber inclusions in a $364 \times 364 \times 364$ voxels portion of the model.

The third point was defined in the precise center of the image stack, and the ROIs grew radially to it. That region was called center region. Figure 5.4 illustrates the center region. The dimensions of the ROIs are listed in Table 5.2.

	ROI-1	ROI-2	ROI-3	ROI-4
Voxels in each dir.	91	182	273	364
Dimension [mm]	0.10	0.20	0.30	0.40
Volume [mm^3]	0.001	0.008	0.027	0.064

Table 5.2: Characteristics of the studied ROIs.

With three Degrees of Freedom (DOF) per node and Periodic Boundary Conditions (PBC) applied, the smallest ROIs generate models with about 2.3e6 DOF, and the biggest ROIs generate models with about 1.4e8 DOF. Using double precision and the PCG method, the memory necessary to analyze the smallest models with the proposed scheme revolves around 98 MB at the bottleneck, while solely storing the whole stiffness matrix as a band symmetric sparse matrix in CSR format would need around 1205 MB. For the biggest models, the scheme proposed allocates around 6273 MB, while solely storing

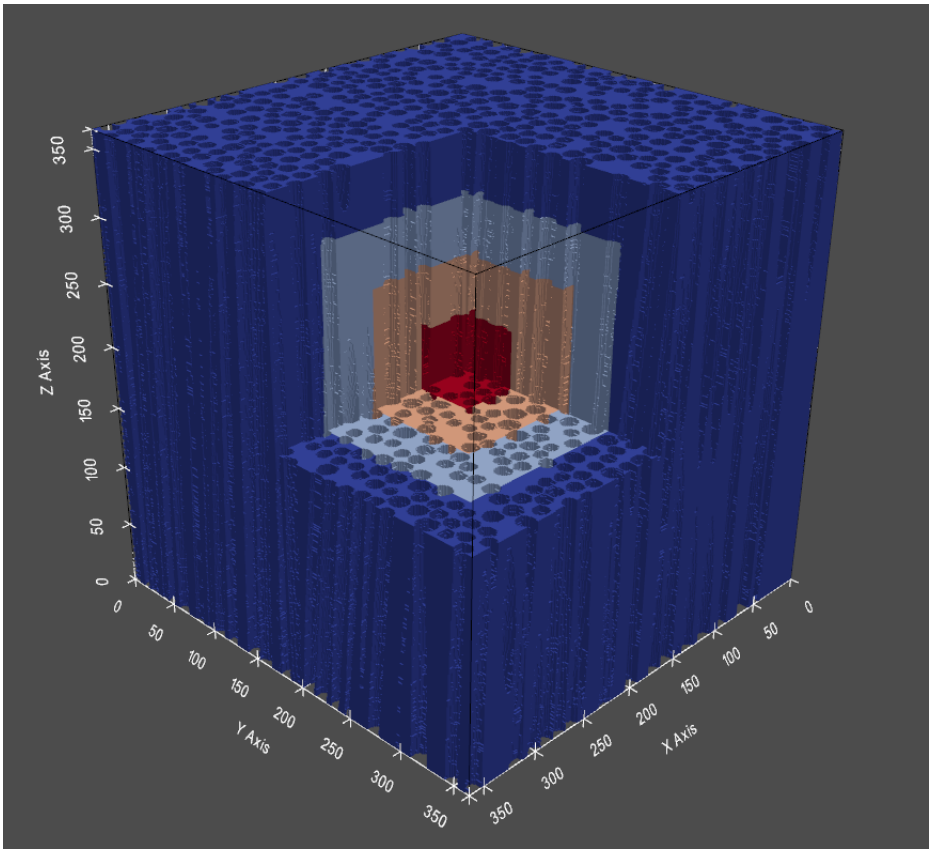

Figure 5.4: Four ROIs spanning from the center of the stack outwards. Only the viscoelastic matrix is shown.

the whole stiffness matrix as a band symmetric sparse matrix in CSR format would need around 73360 MB. As the examples show, the assembly-free strategy is responsible for diminishing in more than 10 times the amount of memory needed to perform the analyses with big models.

The proposed homogenization scheme was applied to all the ROIs and the convergence was analyzed. The material properties used were the same as the second example from the previous chapter, and are described in Tables 4.3 and 4.4.

The results among the three regions analyzed were close enough to indicate that the scanned volume can be perceived as an homogeneous sample at the macroscale. The desired property calculated at any part of the image stack has the same value, provided the ROI is big enough. In addition, in all directions of all the three regions, the relaxation modulus converged as the ROI grew. With other words, the total volume analyzed was sufficient to capture well the material behavior. As the FRP studied was only segmented in two phases, matrix and inclusions, and the average diameter of the fibers is much smaller than the dimensions of the ROIs, the results were as expected.

The transversely isotropic nature of the unidirectional FRP was also correctly perceived by the analyses, likewise the second example. The stiffer direction is the one to which the elastic fibers are aligned, besides being the one with less influence of the viscoelastic nature of the matrix. The other two directions present in general lower stiffness, and are much more prone to relaxation.

The master curves of the three normal relaxation moduli are shown in Figures 5.5, 5.6, and 5.7 for the front top left corner ROIs, in Figures 5.8, 5.9, and 5.10 for the centered ROIs, and in Figures 5.11, 5.12, and 5.13 for the back bottom right ROIs.

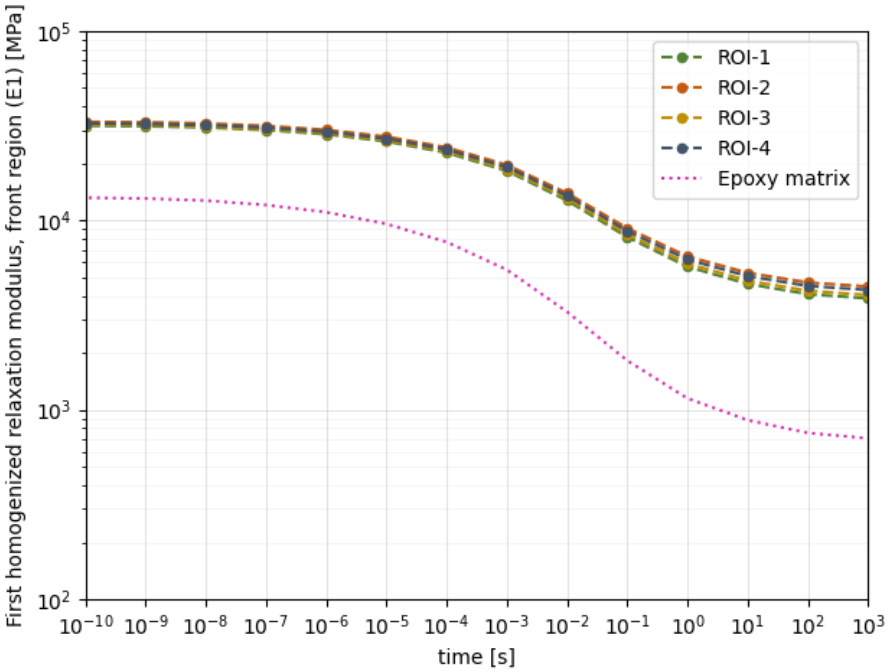

Figure 5.5: Relaxation modulus, E_1, for the ROIs at $(0, 0, 0)$.

As the material was considered homogeneous and transversely isotropic, the Prony series parameters were calculated using only the data from the biggest centered ROI. The procedure was the same as the one performed for the second example from the previous chapter. The results are presented in Table 5.3.

5.2 Asphaltic concrete

Asphaltic concrete (AC) is one of the most used building materials in infrastructural engineering. It is a composite material generally made of a mixture of asphalt binder, mineral aggregates, filler materials, air-filled voids and additives. Two of these constituents play a key role in defining the material characteristics: the binder and the aggregates. The

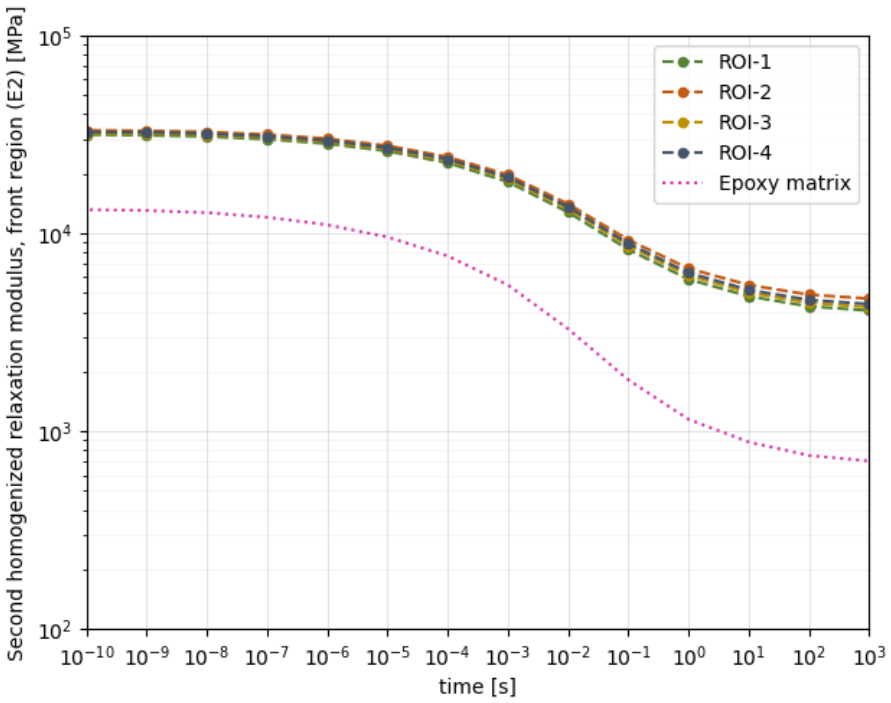

Figure 5.6: Relaxation modulus, E_2, for the ROIs at $(0, 0, 0)$.

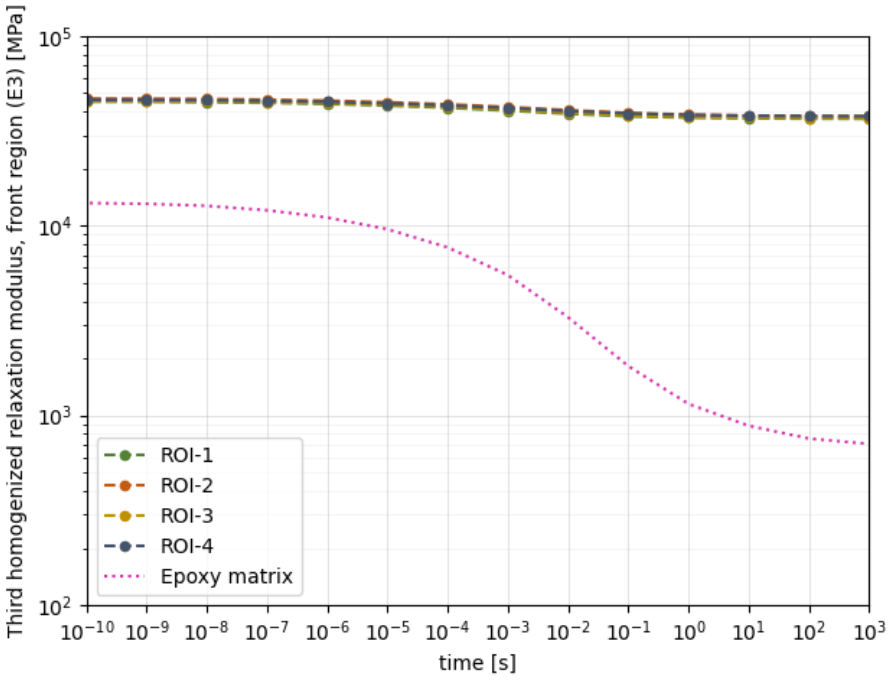

Figure 5.7: Relaxation modulus, E_3, for the ROIs at $(0, 0, 0)$.

rheological nature of the binder adds a property to the material that makes its response to loading dependent to the rate of the load as well as of its magnitude. The aggregates, on the other hand, work as elastic inclusions due to their high stiffness and independency to the rate and duration of the load. AC can then be perceived as a composite made of

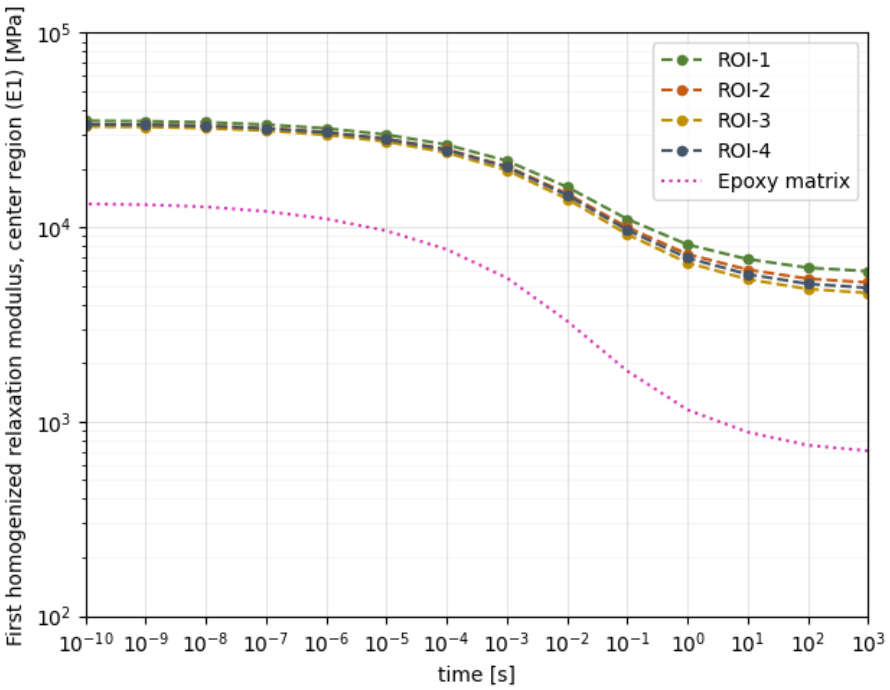

Figure 5.8: Relaxation modulus, E_1, for the ROIs at the center of the stack.

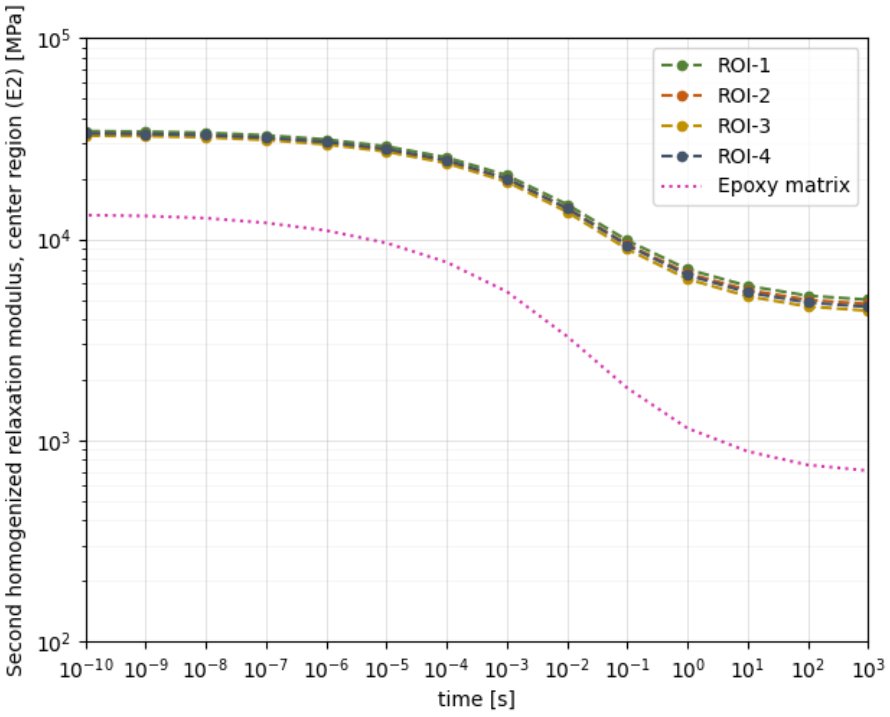

Figure 5.9: Relaxation modulus, E_2, for the ROIs at the center of the stack.

elastic inclusions and air voids embedded in a viscoelastic matrix, hence being prone to be characterized by the scheme proposed in this work.

Three different mixtures of AC were characterized to validate the scheme based on

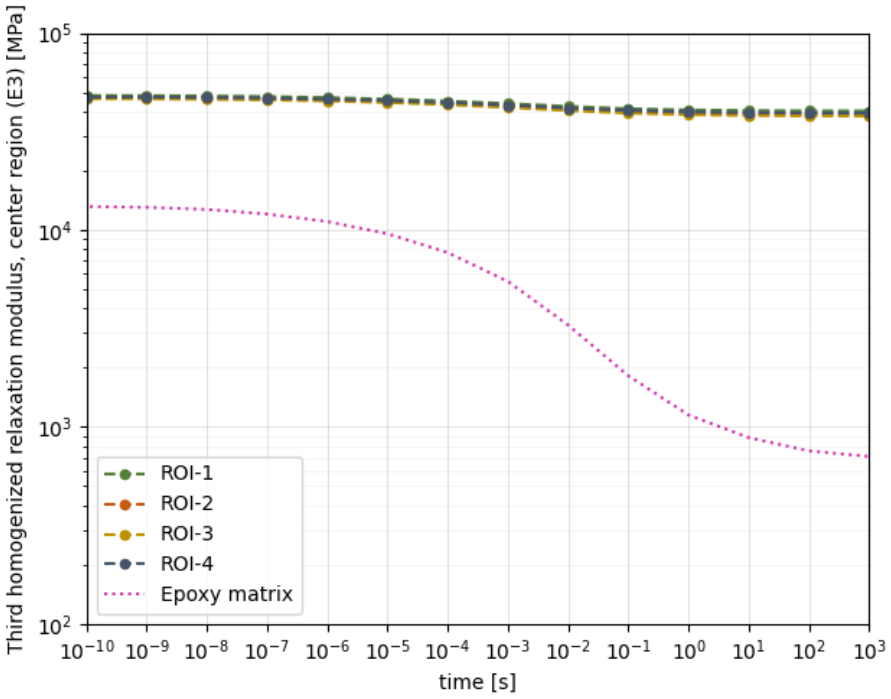

Figure 5.10: Relaxation modulus, E_3, for the ROIs at the center of the stack.

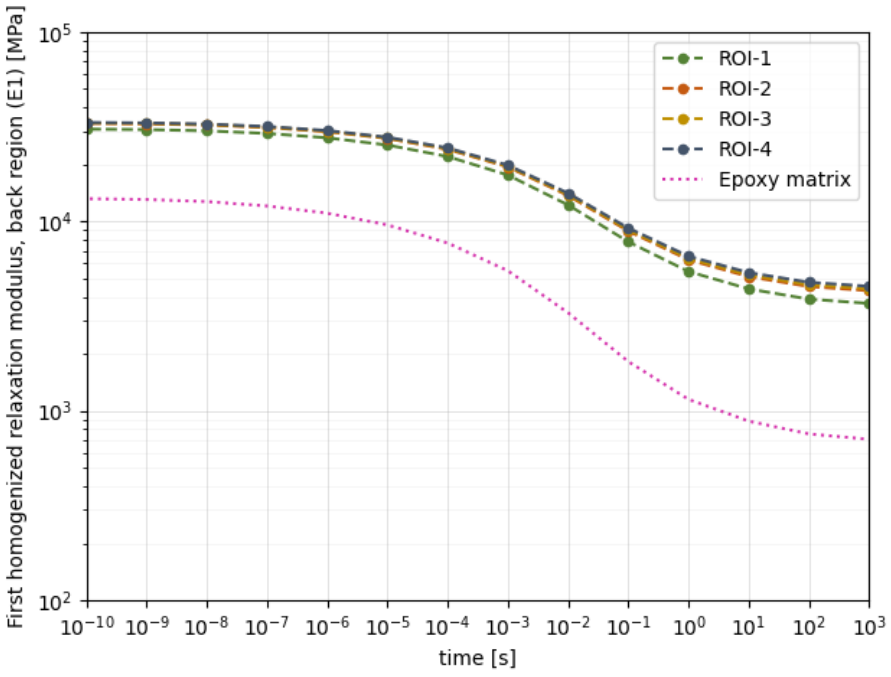

Figure 5.11: Relaxation modulus, E_1, for the ROIs at (end, end, end).

X-ray micro-CT scans of physical samples. The input data came from both the literature (for the aggregate phase) and from experimental tests (the viscoelastic matrix). The results were compared to results from experimental tests with actual samples of the AC mixtures studied. The procedure went as follows in the next sections.

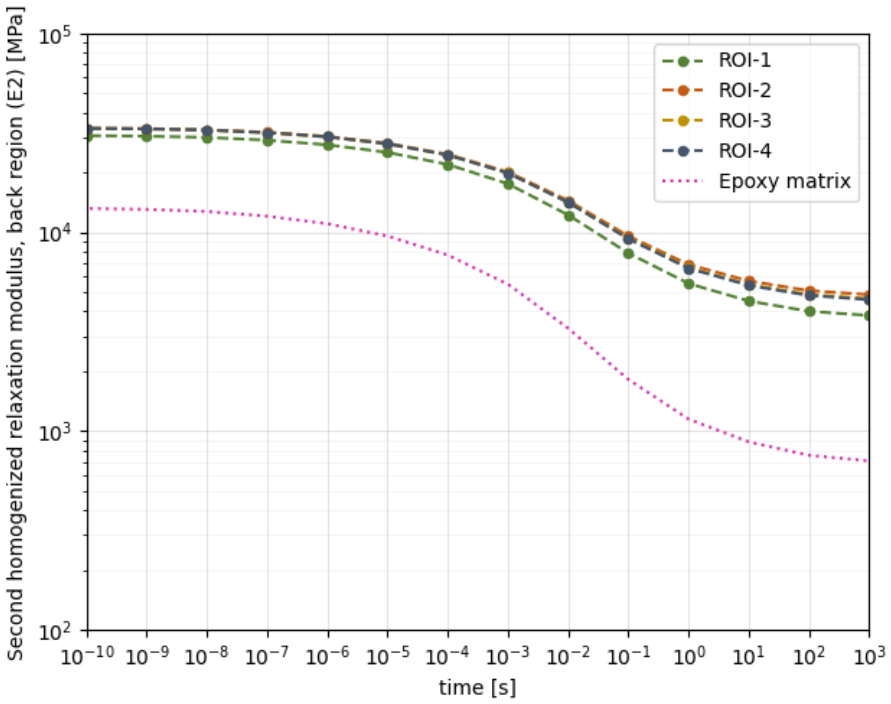

Figure 5.12: Relaxation modulus, E_2, for the ROIs at (end, end, end).

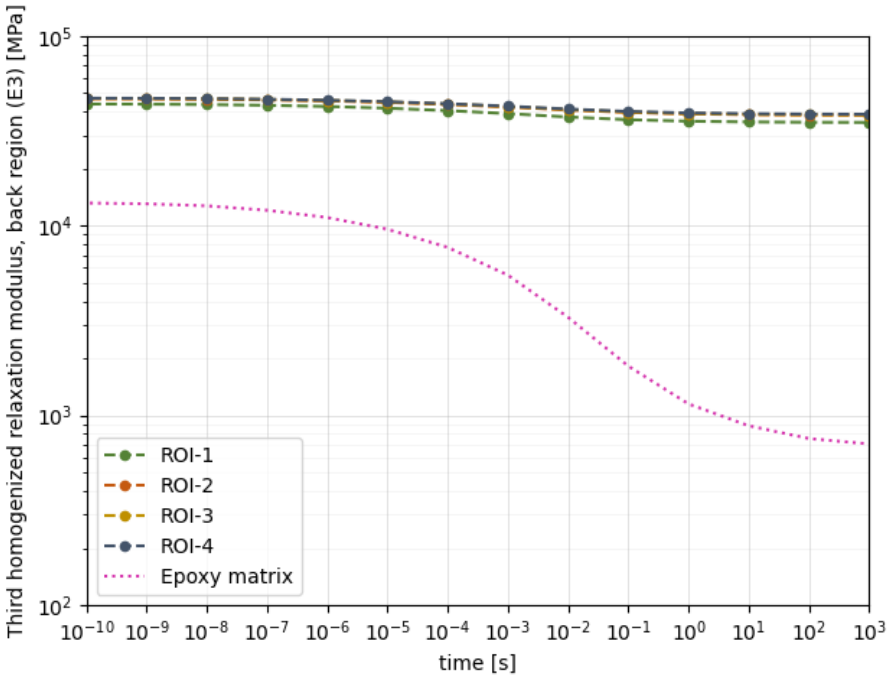

Figure 5.13: Relaxation modulus, E_3, for the ROIs at (end, end, end).

5.2.1 Material preparation and physical analysis

This study used a PG 64S-22 asphalt binder and a gneiss aggregate to fabricate AC and Fine Aggregate Matrix (FAM) samples. Three ACs with distinct nominal maximum

		E^i [MPa]					
i	τ^i [s]	E_1	E_2	E_3	G_{23}	G_{13}	G_{12}
1	1.0e−9	375.8	384.8	392.5	91.8	102.1	92.33
2	1.0e−8	247.1	251.2	392.5	20.11	17.98	14.48
3	1.0e−7	1348	1375	392.5	241.5	204.7	264.6
4	1.0e−6	1394	1370	392.5	305.7	333.5	276.9
5	1.0e−5	2739	2801	796.3	471.5	473.2	513.9
6	1.0e−4	3526	3512	1346	610.6	590.1	575.4
7	1.0e−3	5062	5141	1049	944.8	954.7	969.3
8	1.0e−2	6501	6478	2001	1043.0	1019	1007
9	1.0e−1	4468	4409	478.5	644.6	685.1	649.1
10	1.0e+0	1823	1797	392.5	314.1	306.6	328.8
11	1.0e+1	570.0	550.4	392.5	81.79	98.75	89.78
12	1.0e+2	14.48	1348	1375	392.5	241.5	204.7
∞	-	4876	4612	39250	1012	1083	702.6

Table 5.3: Prony series parameters for the composite homogenized relaxation moduli. Results for the ROI-4 at the center of the stack.

aggregate size (NMAS), i.e., 9.5 mm, 12.5 mm, and 19 mm, with binder contents of 5.8%, 5.3%, and 4.3%, respectively, were produced. These ACs were named AC1, AC2, and AC3, respectively. Associated to each AC, one FAM mixture was designed to serve as input for the analyses. They were named FAM1, FAM2, FAM3, and had binder contents of 7.5%, 7.1%, and 6.1%, respectively. The NMAS of all FAMs was 2.36 mm. It is worth noting that the FAM mixture design process is not yet internationally determined and is in continuous evolution. The data acquired for this work with the physical tests hence serve solely as an application of the proposed numerical scheme, rather then a precise and well-defined manner to characterize the material.

The groups of FAM and AC were characterized by dynamic cyclic tests; the first one to be used as input for the analyses, and the latter to serve as comparison between the computational solutions and experimental results. The elastic characteristics of the aggregate phase were measured experimentally and compared to available data the literature.

5.2.1.1 Aggregate elastic properties

The characteristics of different types of rocks may vary greatly depending on the location of the sample extraction. However, mechanical properties of formations that are considered equivalent worldwide generally stay between a certain and well-defined range. Such is the case of the metamorphic gneiss rock formations. The aggregates used in the FAM and AC sample manufacture was made of gneiss rocks, and for this reason the elastic

properties used in the analysis were defined from the ranges available in several works in the literature [1, 19, 24]. The elastic modulus of the aggregate was also measured using the microindentation technique to confirm the determined value. Three aggregate particles were embedded in resin, grinded and polished to obtain reliable and repeatable indentation measurements. The results of the microindentation tests were found within the range supported by the literature.

The values used for the elastic aggregates are described in Table 5.4.

Elastic properties	
ν	0.24
E [MPa]	50000.0

Table 5.4: Elastic properties of the gneiss aggregates.

5.2.1.2 FAM viscoelastic properties

FAM is a mixture of a viscoelastic binder and small grains of aggregate. It plays the part of binding matrix between the aggregates in the AC. Once the AC is loaded to a point that generates microcracks within the body, that is, damage occurs, it is noticeable that the failure mechanisms take place due to the cohesive damage within the FAM, rather than due to adhesive damage at the interface between the grains and the binder. For this reason, studying the FAM behavior is of utmost importance in characterizing AC mixtures.

One specimen of each FAM measuring 150 mm in diameter and 80 mm in height was fabricated. After the compaction, the samples were cut in a circular saw to reach 50 mm in height and extracted using a drill with an inner diameter of 25 mm, consequently obtaining small FAM specimens. Then, three small replicates of each FAM containing 4.5%±0.5% of air voids were selected to obtain the complex modulus $|E^*|$ of the FAMs, using a servo-hydraulic testing machine. The complex modulus is composed of the real and imaginary parts of the relaxation complex function:

$$|E^*| = E' + iE'' \quad , \tag{5.1}$$

with E' and E'' as defined in Equations 2.22 and 2.23.

The $|E^*|$ of the FAM mixtures was characterized based on uniaxial loading frequency sweep tests. The following testing conditions were applied: frequencies of 25 Hz, 10 Hz, 5 Hz, 1 Hz, 0.5 Hz, and 0.1 Hz, from the highest to the lowest, and temperatures of 4 °C,

and 20 °C, from the lowest to the highest. To guarantee the linearity of the viscoelastic responses, the magnitudes of the haversine cyclic loads were adjusted for each combination of frequency and temperature to ensure the application of strain levels between $50\mu\varepsilon$ and $75\mu\varepsilon$ [43]. The values of $|E^*|$ found were then converted to Prony series parameters to interpolate the relaxation master curve. The Prony series parameters of the three FAM mixtures are described in Table 5.5.

		E^i [MPa]		
i	τ^i [s]	FAM1	FAM2	FAM3
1	2.0e−10	144.3	295.8	451.2
2	2.0e−9	260.3	472.9	694.1
3	2.0e−8	478.0	768.8	1086
4	2.0e−7	861.0	1218	1657
5	2.0e−6	1497	1852	2427
6	2.0e−5	2441	2633	3334
7	2.0e−4	3539	3364	4142
8	2.0e−3	4183	3656	4413
9	2.0e−2	3586	3174	3769
10	2.0e−1	2039	2103	2405
11	2.0e+0	784.0	1070	1100
12	2.0e+1	240.1	450.5	368.4
13	2.0e+2	73.11	176.2	100.2
14	2.0e+3	25.23	70.94	25.87
15	2.0e+4	10.07	30.97	7.275
16	2.0e+5	4.505	14.76	2.389
17	2.0e+6	2.173	7.576	0.925
18	2.0e+7	1.091	4.071	0.411
19	2.0e+8	0.581	2.383	0.212
20	2.0e+9	0.238	0.952	0.080
21	2.0e+10	0.382	2.143	0.176
∞	-	16.72	30.33	0.594

Table 5.5: Prony series parameter that describe the relaxation master curve of FAMs 1, 2, and 3.

The FAMs Poisson's ratio was considered time-independent, and its adopted value was 0.3, as described in [17].

Figure 5.14 showcases the FAM master curves alongside the elastic aggregates constant Young's modulus.

5.2.1.3 AC viscoelastic properties

Three specimens containing 5.5%±0.5% of air voids of each AC mixture, measuring 100 mm in diameter and 150 mm in height, were fabricated to obtain the complex modulus

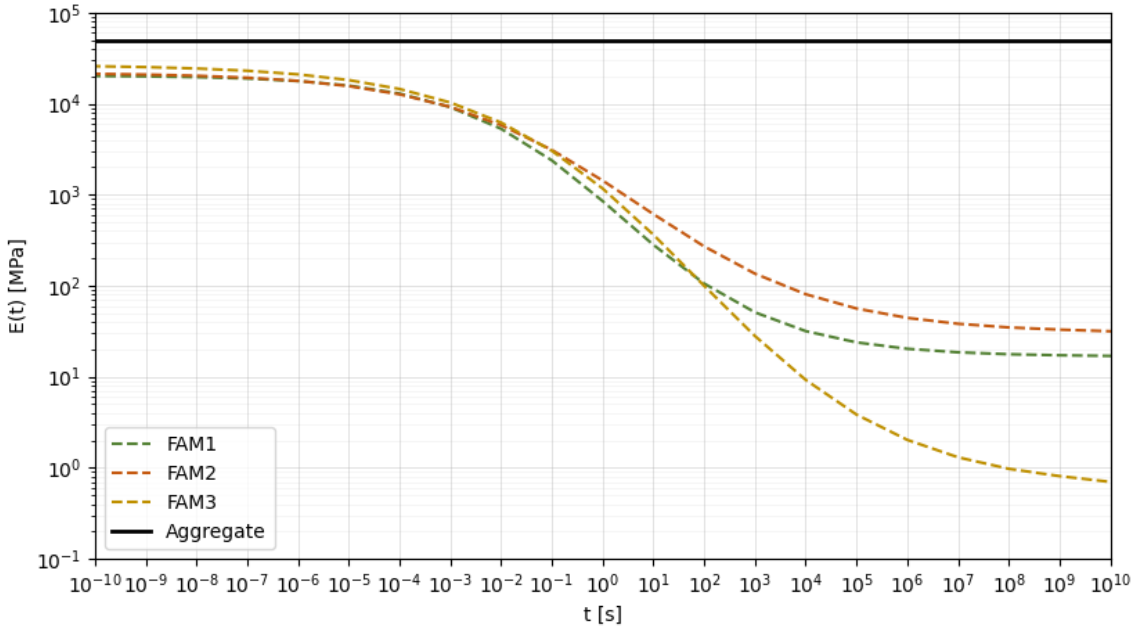

Figure 5.14: Experimental master curves of the three FAM mixtures, and the aggregates' constant Young's modulus.

$|E^*|$ of the ACs. The $|E^*|$ of the AC mixtures were characterized based on uniaxial loading frequency sweep tests, using a servo-hydraulic testing machine. The values of $|E^*|$ found were then converted to Prony series parameters to interpolate the relaxation master curve. The Prony series parameters of the three ACs are described in Table 5.6.

5.2.2 Image acquisition and segmentation

Three specimens of AC with 25 mm in diameter and 50 mm in height were scanned using an Xradia Versa 510 micro-CT device: one specimen of AC1, one of AC2, and one of AC3. The scans generated images with a voxel size of 13 μm. Figure 5.15 shows part of a raw micro-CT scan of asphaltic concrete. The digital image processing was performed using the open source and commercial programs Fiji ImageJ and Dragonfly, respectively. After the preprocessing, each image stack was segmented into three distinct phases: air voids, coarse aggregates, and fine aggregate matrix. Due to the highly heterogeneous nature of the ACs, many filters were applied in the processing of the images and artificial intelligence techniques were used for the properly separating the phases. Figures 5.16 and 5.17 portray examples of single-phase segmentations of air voids and aggregate grains, respectively.

Two strategies were used to validate the segmentation: air void content and aggregate size distribution. Firstly, the air void content obtained by means of the micro-CT scanning

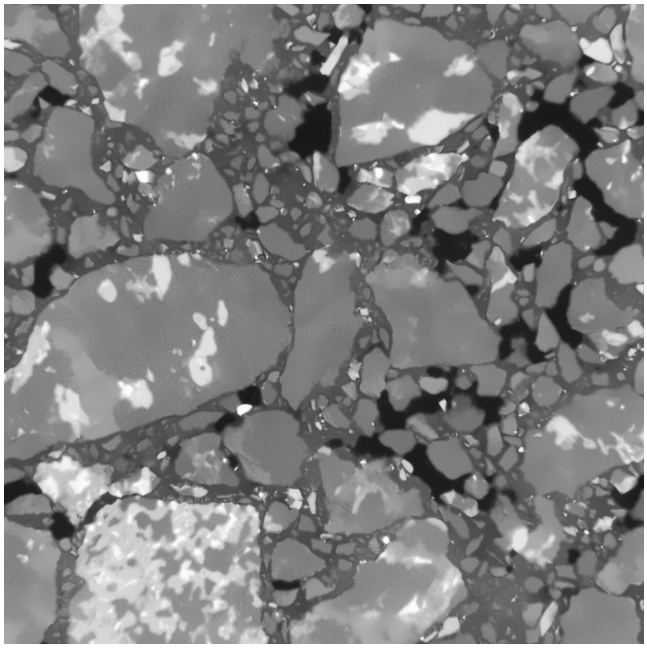

Figure 5.15: Example of a raw micro-CT scan of asphaltic concrete.

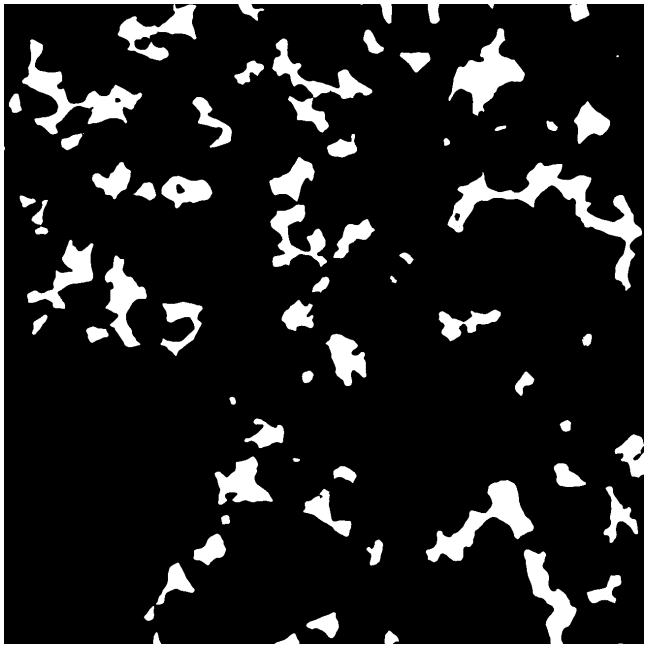

Figure 5.16: Example of a single-phase segmentation of air voids in an asphaltic concrete sample.

		E^i [MPa]		
i	τ^i [s]	AC1	AC2	AC3
1	2.0e−10	79.56	76.51	120.6
2	2.0e−9	158.6	155.0	229.8
3	2.0e−8	322.5	320.5	447.2
4	2.0e−7	647.7	655.8	860.0
5	2.0e−6	1270	1315	1618
6	2.0e−5	2370	2526	2919
7	2.0e−4	4010	4446	4850
8	2.0e−3	5595	6564	6910
9	2.0e−2	5547	6927	7494
10	2.0e−1	3458	4427	5434
11	2.0e+0	1396	1674	2530
12	2.0e+1	452.4	462.0	856.7
13	2.0e+2	150.2	128.4	268.1
14	2.0e+3	56.30	42.10	92.29
15	2.0e+4	23.53	16.15	36.33
16	2.0e+5	10.56	6.875	15.90
17	2.0e+6	4.931	3.105	7.449
18	2.0e+7	2.345	1.442	3.615
19	2.0e+8	1.153	0.695	1.840
20	2.0e+9	0.465	0.278	0.750
21	2.0e+10	0.584	0.336	1.053
∞	-	96.72	44.36	70.21

Table 5.6: Prony series parameter that describe the relaxation master curve of ACs 1, 2, and 3.

was compared to volumetric measurements from the laboratory. Then, a simple sieving algorithm based on the 3-D representation of the aggregates was developed to evaluate the gradation of the particles.

5.2.2.1 Air void analysis

Table 5.7 indicates the air void percentage in each of the samples analyzed, both measured in the laboratory, and the segmented from the micro-CT scans. It is clear that the three samples arrived to a good standard in the air void phase segmentation.

Sample	NMAS [mm]	Binder %	AV % (laboratory)	AV % (micro-CT)
1	9.5	5.76	3.82	3.76
2	12.5	5.34	5.76	5.04
3	19.0	4.3	5.07	6.39

Table 5.7: Comparison between the air void contents of the three AC samples measured in the laboratory and from the micro-CT images.

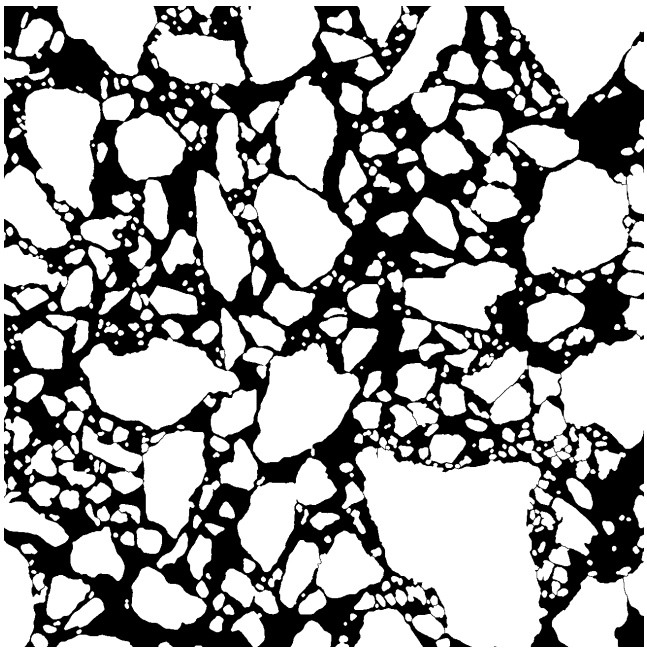

Figure 5.17: Example of a single-phase segmentation of aggregate grains in an asphaltic concrete sample.

5.2.2.2 Aggregate size analysis

The use of a sophisticated algorithm to determine particle size from AC images is unfeasible due to the high number of grains in the mixtures. For this reason, a simple strategy based on the coordinates of the segmented particles was developed and applied to sieve the aggregates.

The strategy consists in simulating a real sieving test, by passing all the segmented aggregate grains through a series of sieves with every time smaller openings. The highest and lowest coordinates of each grain, in each direction, are used to determine the smallest box in which that grain would fit. The dimensions of that box are then considered the dimensions of the grain. Starting with the highest sieve, all three dimensions of every grain are compared to the sieve's opening size. As a real sieve is a two-dimensional mesh, if two or more of the grain dimensions are larger than the opening size, that grain is considered retained at that sieve. If not, it passes on to the next with a smaller opening. In this way, all the segmented aggregates would be labeled as retained in one sieve – or none, if its dimensions are smaller than the smallest opening (what in reality would mean they are retained at the bottom). With all the grains properly sieved, a volume-based granulometric curve can then be created using the number of aggregate voxels retained at each sieve. This is an extremely simplified method for determining grain size distribution, but economic in terms of memory allocation and time processing. Given the number of

particles in the image stacks, it was shown adequate and workable for this case. The sieving results were satisfactory to what was expected. The sieve openings simulated were the same used in the laboratory, that being 25 mm, 19 mm, 12.5 mm, 9.5 mm, 4.75 mm, 2.36 mm, 1.18 mm, 0.59 mm, 0.30 mm, 0.15 mm, and 0.075 mm.

The sieving strategy described above was implemented in Python language to be handle the segmented images in TIF format. Algorithm 2 describes the procedure implemented to sieve all the particles in the image stack.

Algorithm 2 Sieving of aggregate particles

Input: Segmented image, sieves of interest.
Output: Volume fraction of aggregates retained at each sieve.
Enumerate and label the aggregate particles.
Assign to array `sieves` the opening sizes of the sieves of interest.
Create empty array `retainedPctg` with the same size of `sieves` (each entry of `retainedPctg` correspond to a sieve tested).
for p in `all particles` **do**
    for *diam* in `sieves` **do**
        Assign to variable `ret_x` the boolean value of (`x_dimension(`p`) >` *diam*).
        Assign to variable `ret_y` the boolean value of (`y_dimension(`p`) >` *diam*).
        if `ret_x` == `ret_y` **then**
            Assign to variable `retained` the boolean value of `ret_x`.
        else
            Assign to variable `retained` the boolean value of (`z_dimension(`p`) >` *diam*).
        end if
        if `retained` **then**
            Find the volume fraction of p in the whole amount of particles and add that value to the corresponding *diam* entry of `retainedPctg`.
            break
        end if
    end for
end for

The input data for the viscoelastic matrix comes from the FAM experimental characterization. All FAMs have a nominal maximum aggregate size of 2.36 mm, so every aggregate particle smaller than 2.36 mm in the segmentation should be incorporated into the viscoelastic binding matrix phase. For this reason, the percentage of passing aggregates in the 2.36 mm sieve is the key to validate the segmentation. A similar percentage of aggregates retained at the 2.36 mm and coarser sieves between the sieving experiment and simulation, means that the segmented images captured well the number of big grains, while the smaller ones are considered part of the viscoelastic matrix. It is important to note that the experimental granulometric analysis is based on the mass retained at each

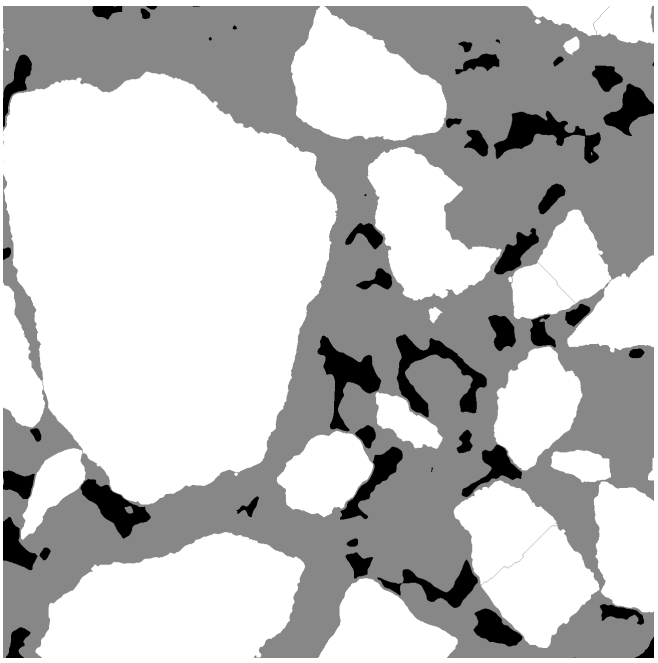

Figure 5.18: Example of fully segmented micro-CT image of asphaltic concrete ready to be used as input to the program. The aggregate grains are the white phase, the air voids are the black phase, and the grey phase is the viscoelastic binding matrix.

sieve, while the strategy proposed here is based on volume. A direct correlation can be done with the simplification of considering the aggregate grains as made of a homogeneous material, with a constant specific mass. Such consideration is not the reality, as aggregate rocks are highly heterogeneous and composed of diverse minerals. However, this simplification is acceptable given the purpose of this work, and is also largely employed in experimental testing and concrete design.

The comparison between the passing percentage of grains through the 2.36 mm in the real experiments and the simulations is shown in Table 5.8. Figure 5.18 shows an example of the final image to be used as input segmented in three phases.

Sample	NMAS [mm]	Sieving test [%]	Sieving simulation [%]
1	9.5	45.00	37.66
2	12.5	38.00	38.02
3	19.0	26.00	18.25

Table 5.8: Comparison of passing aggregate percentage in the three samples between the experimental data and micro-CT segmentation.

The raw image processing and segmentation were performed with the original resolution of 13 μm/voxel, but for the numerical simulations, the images were coarsened to the resolution of 35 μm/voxel because of memory limitations.

5.2.2.3 ROI definition

Likewise the previous example with the FRP composite, several ROIs were extracted from three different regions of each image stack. As the samples were cylinders, all ROIs were centered at its axis, growing outwards radially. The three regions picked for the analysis were the top face of the sample, the bottom face of the sample, and the middle of the sample. The size of the extracted ROIs is available in Table 5.9

Edge size of the cubical ROIs in each region of the stack		
ROI	Size in voxels	Size in cm
1	143	0.50
2	214	0.75
3	286	1.00
4	357	1.25
5	429	1.50
6	500	1.75

Table 5.9: ROI characteristics from the images at the resolution of 35 μm/voxel.

The AC samples were designed to be cylinders with 25mm in diameter, but inaccuracies come from imperfections in manufacturing. As a consequence, the ROIs with 1.75cm in edge size were the biggest attainable from the micro-CT scans.

5.2.3 Results and discussion

The experimental dynamic moduli $|E^*|$ were transformed from the frequency to the time domain using the equations presented in Subsection 2.1.2. With the Prony series parameters of the binding matrix defined in the time domain, the homogenization procedure can be carried on.

Figures 5.19, 5.20, and 5.21 show the relaxation modulus master curves in all three directions of the biggest centered ROI of the three samples. Table 5.9 presents the calculated values at the beginning and the end of the curves, and the standard deviation among the three directions for each of the presented samples. The results show that all AC mixtures, in practical terms, can be considered isotropic. The master curves in all three directions have the same shape and closely match values within the same order of magnitude at all instants. The same behavior was found for every other region of the samples. For this reason, the following comments on the numerical results take into account the relaxation modulus in the samples' axial direction, which was the one tested in the laboratory.

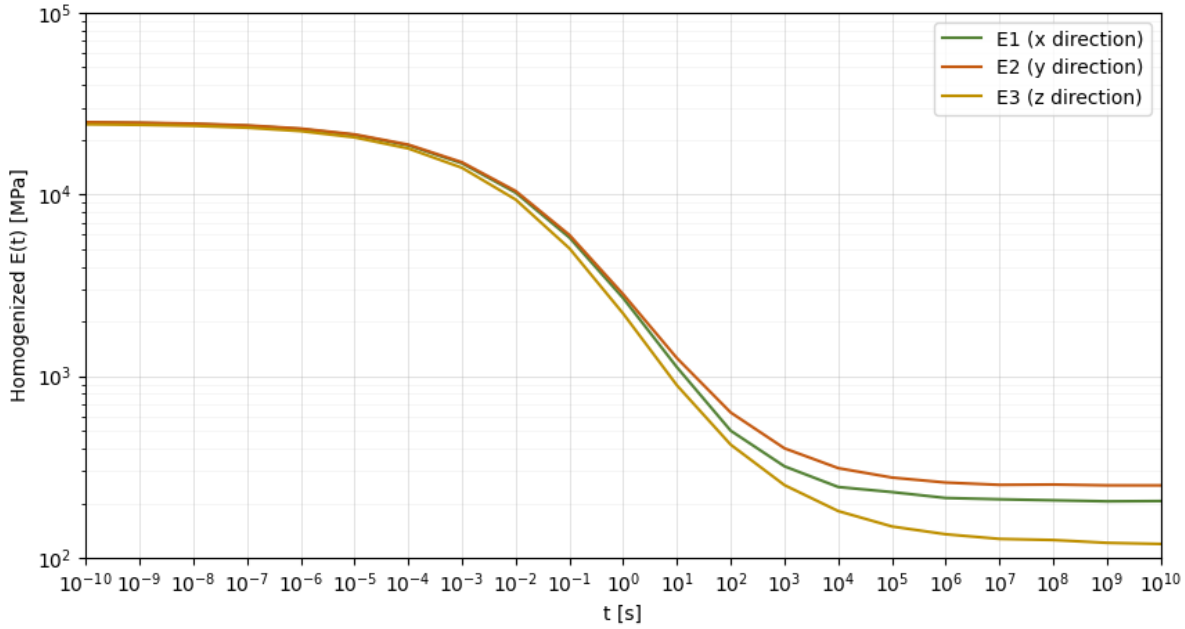

Figure 5.19: Relaxation moduli calculated for the centered ROI-6 of AC1.

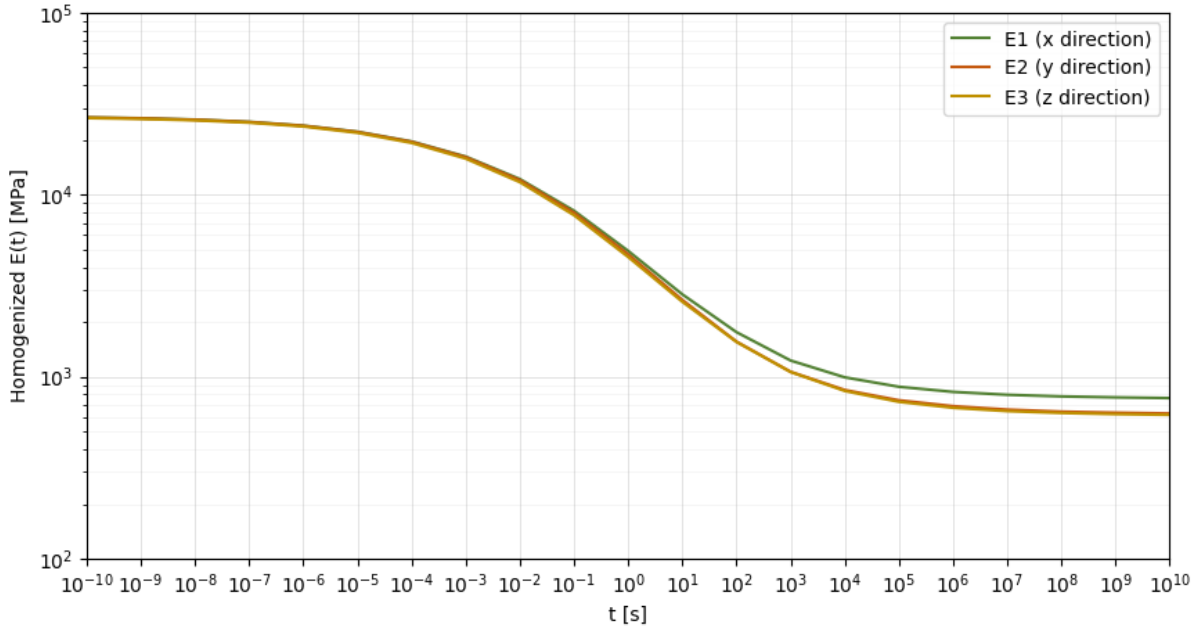

Figure 5.20: Relaxation moduli calculated for the centered ROI-6 of AC2.

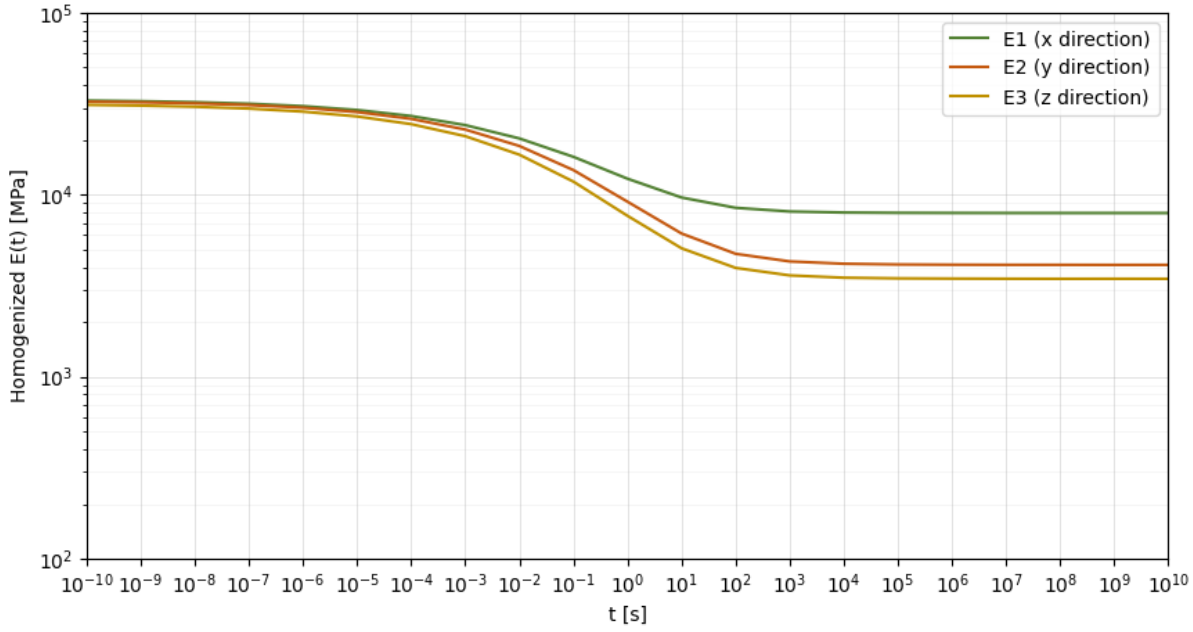

Figure 5.21: Relaxation moduli calculated for the centered ROI-6 of AC3.

	Sample 1			Sample 2			Sample 3		
t	E_1	E_2	E_3	E_1	E_2	E_3	E_1	E_2	E_3
1e-11 s	2.49e4	2.50e4	2.43e4	2.67e4	2.66e4	2.64e4	3.30e4	3.25e4	3.12e4
S.D.	2.89e2			9.92e1			7.32e2		
Coef. of var.	1.17%			0.37%			2.27%		
1e11 s	2.02e2	2.51e2	1.18e2	7.58e2	6.22e2	6.13e2	7.93e3	4.12e3	3.45e3
S.D.	5.47e1			6.62e1			1.97e3		
Coef. of var.	28.76%			9.97%			38.19%		

Table 5.10: Analysis of the results at the beginning and at the end of the master curves of the biggest centered ROI. The relaxation moduli and standard deviations are in MPa.

The convergence analyses performed took account of the standard deviation for each size of ROI among the three regions of each sample. To exemplify the behavior found in all samples, Table 5.11 presents the average of E_3 in the three regions from the analysis of ROIs 2, 4, and 6 of sample 2 at some instants.

Table 5.11 shows that the coefficient of variation of the relaxation moduli diminishes as the size of the ROI grows, in the whole curve, for the most significant cases. This supports the fact that a ROI needs to contain at least a certain amount of the material to be representative. The closer the ROI volume gets to this minimum, the closer the calculated property approaches the real homogenized value. For this work, the biggest cubic ROI attainable measured 1.75 cm in side because of limitations in the sample

	ROI-2			ROI-4			ROI-6		
t	Mean E_3	S.D.	Coef. of var.	Mean E_3	S.D.	Coef. of var.	Mean E_3	S.D.	Coef. of var.
1e-11 s	2.86e4	3.35e3	11.72%	2.65e4	3.44e3	12.96%	2.70e4	1.85e3	6.84%
1e-5 s	2.44e4	3.85e3	15.78%	2.20e4	3.46e3	15.69%	2.24e4	1.83e3	8.17%
1e0 s	7.68e3	4.73e3	61.59%	4.79e3	1.71e3	35.65%	4.80e3	7.81e2	16.29%
1e5 s	3.58e3	4.29e3	119.86%	9.00e2	6.79e2	75.40%	8.92e2	3.17e2	35.56%
1e11 s	3.45e3	4.28e3	124.11%	7.71e2	6.42e2	83.27%	7.70e2	2.97e2	38.62%

Table 5.11: Convergence analysis of the results calculated with different ROIs at some instants. The means and standard deviations are in MPa.

manufacturing. That is a small volume when compared to the maximum aggregate size of the ACs, especially AC3, that had NMAS of 19 mm. However, for all the three samples analyzed, the coefficient of variation stayed below 50% at their biggest ROI. Enlarging the sample volume wouldn't make the results much more representative given the achievable quality of the images. So, the volume of material used was considered large enough for the purposes of this study.

With the AC samples containing a rather small percentage of air voids, and incorporating into the matrix phase the grains smaller than 2.36 mm, the aggregate phase remains as a large portion of the images. Table 5.12 presents the percentage of the segmented phases of the samples after the digital sieving described in Section 5.2.2.2. As the aggregates are elastic inclusions in the viscoelastic matrix, their contribution to the homogenized stiffness is constant in time. At the beginning of the time span, the relaxation moduli of the FAMs closely match the Young's modulus of the aggregates, making them almost equally influential in the determination of the AC homogenized stiffness. However, as the time marches on, the relaxation moduli of all matrix mixtures decrease in more than one order of magnitude, giving the elastic inclusions a much more defining role in the determination of the AC homogenized stiffness. This relation occurs because the FE modeling considers the interface between the grains and the matrix bonded during the whole period – that is, no adhesive damage occurs. In that sense, a higher percentage of elastic phase means a higher stiffness in the long-term instants, as well as a less evident propension to the FAM relaxation. These differences are observable in Figure 5.22, which shows the relaxation master curve of the biggest centered ROI of the three samples, as well as the ones of their corresponding FAMs. It is noticeable that after the relaxation modulus of the FAM decays in about two orders of magnitude, its influence in the homogenized master curve becomes every time less prominent, giving place to the steadiness of the elastic inclusion's constant stiffness. This behavior is especially expressive in sample 7. The ex-

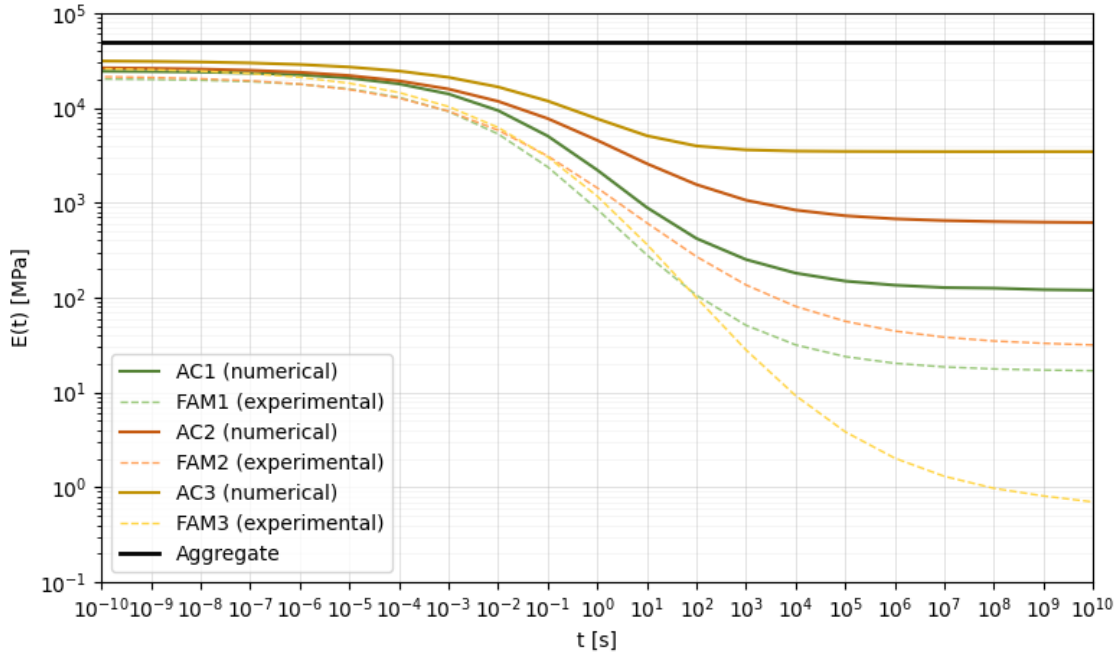

Figure 5.22: Master curves of the homogenized relaxation modulus of the three samples, of the three experimental FAMs, and the constant aggregate Young's modulus.

perimental testing and data treatment couldn't capture the complex modulus that would stabilize the long-term value of the FAM3 relaxation master curve, but the decay becomes irrelevant. The relaxation modulus of the FAM by the end of the studied period is much smaller than the aggregate Young's modulus, so the homogenized stiffness is already stabilized by then. Figures 5.23, 5.24, and 5.25 display the numerical results of all samples

Phase %	Sample 1	Sample 2	Sample 3
Air voids	3.76	5.04	6.39
FAM	51.39	60.67	31.03
Aggregates	44.85	34.29	62.58

Table 5.12: Percentage of segmented phases of the AC samples after the digital sieving.

in comparison with their related experimental AC and FAM measurements. The full line curves plotted are the average values between the three regions (top, center, bottom) of the biggest ROIs of each sample. It is noticeable that the percentage of aggregates in the segmented images is the preponderant factor in determining the curve shape. Also worth noting is that, with this formulation, the higher the difference between the stiffness of the constituents, the more emphasis is given to the stiffer material in determining the homogenized stiffness. Afterall, all the segmented images present a high percentage of aggregates, given that all long term relaxation moduli were determined higher than the defined by the laboratory data.

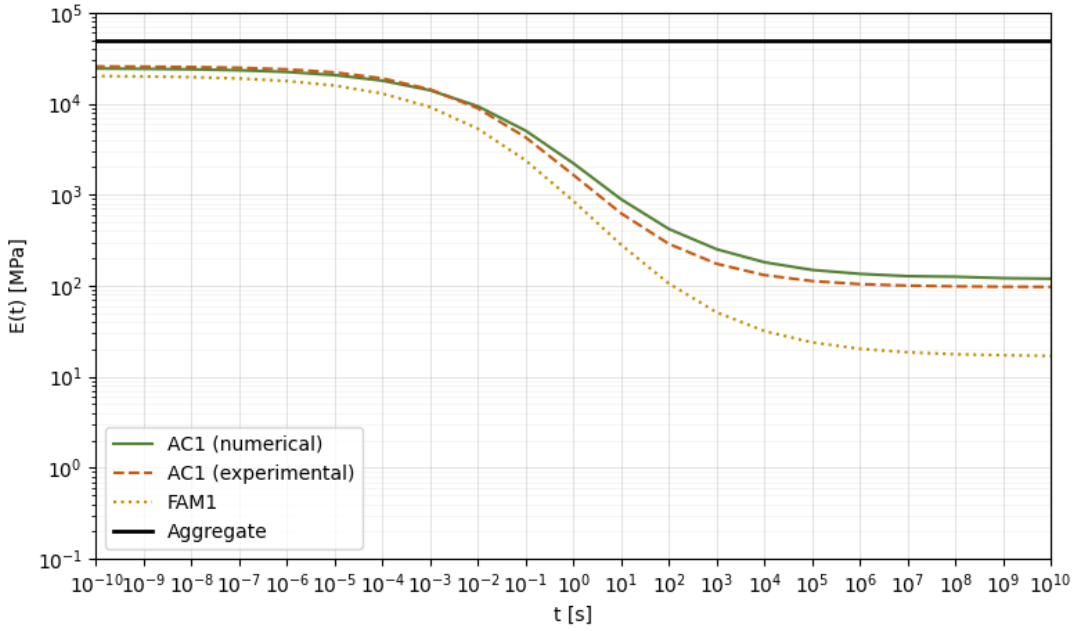

Figure 5.23: Master curves of the homogenized relaxation modulus of the Sample 1, AC1, FAM1, the constant aggregate Young's modulus.

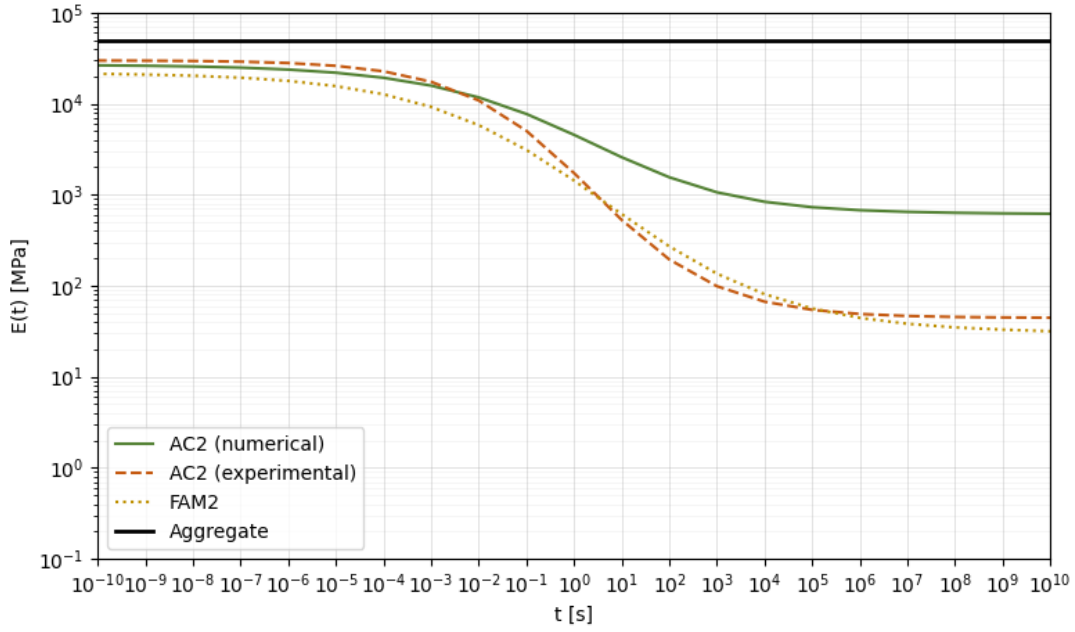

Figure 5.24: Master curves of the homogenized relaxation modulus of the Sample 2, AC2, FAM2, the constant aggregate Young's modulus.

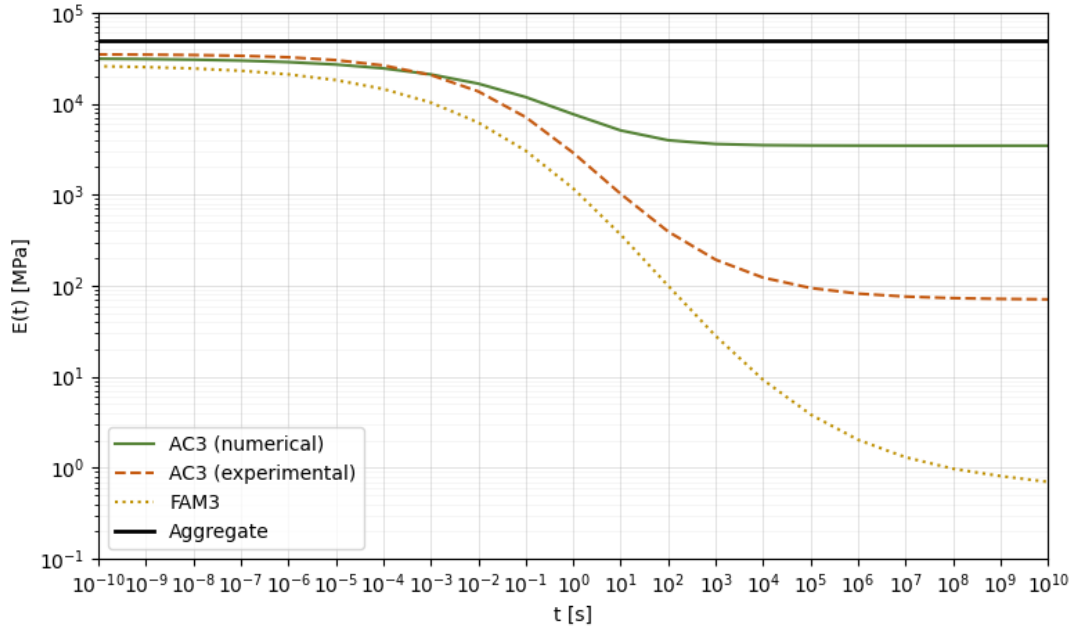

Figure 5.25: Master curves of the homogenized relaxation modulus of the Sample 3, AC3, FAM3, the constant aggregate Young's modulus.

The inaccuracy between the numerical and experimental results can be explained with two reasons. First, the whole laboratory testing procedure and experimental data treatement conducted carry out inherent inaccuracies and hence do not perfectly represent the material. In addition, the large span of time covered by the Prony series prevents the proper definition of the long term stiffness of the mixtures. The AC2 master curve also didn't follow the expected shape throughout the whole time span covered, conveying that, at some instants, the asphaltic concrete would be less stiff than the fine aggregate matrix.

The second reason is the quality of the image segmentations. The diversity of minerals inside each aggregate rock as well as the geometric arrangement of the AC constituents within each sample make the micro-CT scans troublesome to precisely segment, especially in few phases, like the cases studied in this work. Additionally, the sieving algorithm applied can't perform well unless the grains' surfaces are properly defined and separated. This requires an exquisite work on the separation of the different phases, which cannot always be done, given the resolution of the micro-CT scans and the size of the particles, as it was the case here.

More precise laboratory procedures and a better quality of images and segmentation would undoubtedly elevate the accuracy in the material representation with the numerical results. However, it is clear that the method proposed is capable of capturing the visco-

elastic nature of asphaltic concrete. For instance, the experimental data of both FAM1 and AC1 behaved well and as expected. The micro-CT images of samples 1 were of good quality and the segmentation was feasible. As a consequence, the numerical results of sample 1 remained at all times within the same order of magnitude as the expected AC1 relaxation master curve.

6 Conclusions

This work introduced a novel image-based scheme for homogenizing viscoelastic properties of heterogeneous materials in the time domain. With the proposed approach, the load history is not required, and the homogenization is performed based solely on the material physical and microstructural characteristics, which are described by the images. The procedure is carried out by applying to the microstructure a constant strain in time, thus simulating a relaxation test over a Representative Volume Element (RVE) of the heterogeneous material.

Two synthetic models were analyzed to verify the method, and two examples of applications to real materials were studied. The first one of them using X-ray micro-CT images of a Fiber-Reinforced Polymer (FRP) composite with input data from the literature. The second application studied used X-ray micro-CT images of three Asphaltic Concrete (AC) samples. The input data used for the elastic aggregates was extracted from the literature, but the viscoelastic properties of the binding matrix were acquired with experimental tests. Finally, the numerical solutions were compared to the experimental data obtained from tests with samples of the same AC mixtures. All the results captured the expected behaviors, thus validating the scheme. In addition, the parameters that adjust the relaxation master curves were calculated through the solution of an optimization problem using the least squares method.

A massive economy in memory necessary for the material characterization using the proposed scheme was observed, what makes it accessible to not so powerful computers, such as PCs. In addition, the memory savings alongside the possibility of parallelization of the scheme provides a great opening to its implementation using GPU-based approaches which would, again, reduce even more dramatically the processing time.

References

[1] Amah, E. A.; Oden, M. I.; Anam, G. S. Effects of weathering on mechanical properties of granite gneiss and dolerite: a case study of oban and obudu basement rocks in south-eastern nigeria. *Global Journal of Geological Science 11* (2013), 37–45.

[2] Barbero, E. J. *Finite Element Analysis of Composite Materials*. CRC Press, 2008.

[3] Bouchedjra, M.; Kanit, T.; Boulemia, C.; Amrouche, A.; Belouchrani, M. E. A. Determination of the rve size for polycrystal metals to predict monotonic and cyclic elastoplastic behavior: Statistical and numerical approach with new criteria. *European Journal of Mechanics - A/Solids 72* (2018), 1–15.

[4] Cavalcante, M. A.; Marques, S. P. Homogenization of periodic materials with viscoelastic phases using the generalized fvdam theory. *Computational Materials Science 87* (2014), 43–53.

[5] Christensen, R. Viscoelastic properties of heterogeneous media. *Journal of the Mechanics and Physics of Solids 17*, 1 (1969), 23–41.

[6] Christensen, R. M. *Theory of Viscoelasticity - An Introduction*, 2nd ed. Academic Press, 1982.

[7] Coulibaly, M.; Sabar, H. Micromechanical modeling of linear viscoelastic behavior of heterogeneous materials. *Archive of Applied Mechanics 81*, 3 (Mar 2011), 345–359.

[8] Dai, Q. Two- and three-dimensional micromechanical viscoelastic finite element modeling of stone-based materials with x-ray computed tomography images. *Construction and Building Materials 25*, 2 (2011), 1102–1114. Composite Materials and Adhesive Bonding Technology.

[9] Ferguson, J. C.; Panerai, F.; Borner, A.; Mansour, N. N. Puma: the porous microstructure analysis software. *SoftwareX 7* (2018), 81–87.

[10] Ferry, J. D. *Viscoelastic Properties of Polymers*. John Wiley & Sons, 1980.

[11] Fish, J.; Belytschko, T. *A First Course In Finite Elements*. John Wiley & Sons, 2007.

[12] Geers, M.; Kouznetsova, V.; Brekelmans, W. Multi-scale computational homogenization: Trends and challenges. *Journal of Computational and Applied Mathematics 234*, 7 (2010), 2175–2182. Fourth International Conference on Advanced COmputational Methods in ENgineering (ACOMEN 2008).

[13] Hashin, Z. Viscoelastic Behavior of Heterogeneous Media. *Journal of Applied Mechanics 32*, 3 (09 1965), 630–636.

[14] Hill, R. Elastic properties of reinforced solids: Some theoretical principles. *Journal of the Mechanics and Physics of Solids 11*, 5 (1963), 357–372.

[15] Kouznetsova, V.; Brekelmans, W. A. M.; Baaijens, F. P. T. An approach to micro-macro modeling of heterogeneous materials. *Computational Mechanics 27*, 1 (Jan 2001), 37–48.

[16] Li, L.; Li, W.; Wang, H.; Zhao, J.; Wang, Z.; Dong, M.; Han, D. Investigation of prony series model related asphalt mixture properties under different confining pressures. *Construction and Building Materials 166* (2018), 147–157.

[17] Li, Y.; Metcalf, J. B. Two-step approach to prediction of asphalt concrete modulus from two-phase micromechanical models. *Journal of Materials in Civil Engineering 17*, 4 (2005), 407–415.

[18] Liu, D. C.; Nocedal, J. On the limited memory bfgs method for large scale optimization. *Mathematical Programming 45*, 1 (Aug 1989), 503–528.

[19] Ljunggren, C.; Stephansson, O.; Alm, O.; Hakami, H.; Mattila, U. Mechanical properties of granitic rocks from gideå, sweden. Tech. rep., Luleå, Sweden, 1985.

[20] Luciano, R.; Barbero, E. J. Analytical Expressions for the Relaxation Moduli of Linear Viscoelastic Composites With Periodic Microstructure. *Journal of Applied Mechanics 62*, 3 (09 1995), 786–793.

[21] Mase, G. T.; Smelser, R. E.; Mase, G. E. *Continuum Mechanincs for Engineers*, 3 ed. CRC Press, Boca Raton, USA, 2010.

[22] Mehdikhani, M.; Breite, C.; Swolfs, Y.; Wevers, M.; Lomov, S. V.; Gorbatikh, L. A dataset of micro-scale tomograms of unidirectional glass fiber/epoxy and carbon fiber/epoxy composites acquired via synchrotron computed tomography during in-situ tensile loading. *Data in Brief 34* (2021).

[23] Michel, J.; Moulinec, H.; Suquet, P. Effective properties of composite materials with periodic microstructure: a computational approach. *Computer Methods in Applied Mechanics and Engineering 172*, 1 (1999), 109–143.

[24] Monticelli, J. P. Weathering study of the gneissic rock mass from the monte seco tunnel region, southeastern brazil. Master's dissertation, Universidade de São Paulo, São Paulo, Brasil, 2019.

[25] Mori, T.; Tanaka, K. Average stress in matrix and average elastic energy of materials with misfitting inclusions. *Acta Metallurgica 21*, 5 (1973), 571–574.

[26] Moussaddy, H.; Therriault, D.; Lévesque, M. Assessment of existing and introduction of a new and robust efficient definition of the representative volume element. *International Journal of Solids and Structures 50*, 24 (2013), 3817–3828.

[27] Naik, A.; Abolfathi, N.; Karami, G.; Ziejewski, M. Micromechanical viscoelastic characterization of fibrous composites. *Journal of Composite Materials 42*, 12 (2008), 1179–1204.

[28] Park, S. W.; Schapery, R. A. Methods of interconversion between linear viscoelastic material functions. part i - a numerical method based on prony series. *International Journal of Solids and Structures 36* (1999), 1653–1675.

[29] Pelissou, C.; Baccou, J.; Monerie, Y.; Perales, F. Determination of the size of the representative volume element for random quasi-brittle composites. *International Journal of Solids and Structures 46*, 14 (2009), 2842–2855.

[30] Penta, R.; Gerisch, A. An introduction to asymptotic homogenization. In *Multiscale Models in Mechano and Tumor Biology* (Cham, 2017), A. Gerisch, R. Penta, and J. Lang, Eds., Springer International Publishing, pp. 1–26.

[31] Pindera, M.-J.; Khatam, H.; Drago, A. S.; Bansal, Y. Micromechanics of spatially uniform heterogeneous media: A critical review and emerging approaches. *Composites Part B: Engineering 40*, 5 (2009), 349–378.

[32] Reddy, J. N. *An Introduction to the Finite Element Method*, 3rd ed. McGraw-Hill, 2006.

[33] Rodríguez-Ramos, R.; Otero, J.; Cruz-González, O.; Guinovart-Díaz, R.; Bravo-Castillero, J.; Sabina, F.; Padilla, P.; Lebon, F.; Sevostianov, I. Computation of the relaxation effective moduli for fibrous viscoelastic composites using the asymptotic homogenization method. *International Journal of Solids and Structures 190* (2020), 281–290.

[34] Schapery, R. A. A simple collocation method for fitting viscoelastic models to experimental data. Tech. rep., 1962.

[35] Schapery, R. A. Viscoelastic behavior and analysis of composite materials. In *Mechanics of Composite Materials*. New York: Academic Press, 1974, ch. 4.

[36] Schindelin, J.; Arganda-Carreras, I.; Frise, E.; Kaynig, V.; Longair, M.; Pietzsch, T.; Preibisch, S.; Rueden, C.; Saalfeld, S.; Schmid, B., et al. Fiji: an open-source platform for biological-image analysis. *Nature methods 9*, 7 (2012), 676–682.

[37] Schüler, T.; Jänicke, R.; Steeb, H. Nonlinear modeling and computational homogenization of asphalt concrete on the basis of xrct scans. *Construction and Building Materials 109* (2016), 96–108.

[38] Selivanov, M. F.; Chernoivan, Y. A. A combined approach of the laplace transform and padé approximation solving viscoelasticity problems. *International Journal of Solids and Structures 44*, 1 (2007), 66–76.

[39] Serra-Aguila, A.; Puigoriol-Forcada, J. M.; Reyes, G.; Menacho, J. Viscoelastic models revisited: characteristics and interconversion formulas for generalized kelvin–voigt and maxwell models. *Acta Mechanica Sinica 35*, 6 (Dec 2019), 1191–1209.

[40] Shewchuk, J. R. An introduction to the conjugate gradient method without the agonizing pain. Tech. rep., USA, 1994.

[41] Souza, F. V. Modelo multi-escala para analise estrutural de compositos viscoelasticos suscetiveis ao dano. Master's dissertation, Universidade Federal do Ceara, Fortaleza, Brasil, 2005.

[42] Tang, T.; Felicelli, S. D. Computational evaluation of effective stress relaxation behavior of polymer composites. *International Journal of Engineering Science 90* (2015), 76–85.

[43] Underwood, B. S. *Multiscale Constitutive Modeling of Asphalt Concrete*. Tese de Doutorado, North Carolina State University, Raleigh, North Carolina, USA, 2011.

[44] Yi, Y.-M.; Park, S.-H.; Youn, S.-K. Asymptotic homogenization of viscoelastic composites with periodic microstructures. *International Journal of Solids and Structures 35*, 17 (1998), 2039–2055.

[45] Ying, H.; Elseifi, M. A.; Mohammad, L. N.; Hassan, M. M. Heterogeneous finite-element modeling of the dynamic complex modulus test of asphalt mixture using x-ray computed tomography. *Journal of Materials in Civil Engineering 26*, 9 (2014), 04014052.

[46] You, T.; Al-Rub, R. K. A.; Masad, E. A.; Kassem, E.; Little, D. N. Three-dimensional microstructural modeling framework for dense-graded asphalt concrete using a coupled viscoelastic, viscoplastic, and viscodamage model. *Journal of Materials in Civil Engineering 26*, 4 (2014), 607–621.

[47] You, Z.; Adhikari, S.; Emin Kutay, M. Dynamic modulus simulation of the asphalt concrete using the x-ray computed tomography images. *Materials and Structures 42*, 5 (Jun 2009), 617–630.

[48] Zienkiewicz, O. C.; Taylor, R. L. *The Finite Element Method*, 5th ed., vol. 1: The Basis. Butterworth-Heinemann, 2000.

[49] Zohdi, T. I. *A Finite Element Primer for Beginners*. Springer, 2015.